Mechanisms of creep in shale from nanoscale to specimen scale

Qing Yin · Yingxiao Liu · Ronaldo I. Borja*

Department of Civil and Environmental Engineering, Stanford University, Stanford, CA 94305, USA. *E-mail: borja@stanford.edu

Summary. Creep in shale is a multiscale deformation process across both space and time. In this paper, we propose a scale-bridging technique linking creep phenomena in shale from nanometer scale to specimen scale, and explore the mechanisms of creep at different scales. To this end, we simulate indentation tests on Woodford shale at the nanometer and micrometer scales using an incremental frictionless multi-body contact algorithm based on the Lagrange multipliers method, along with a recently developed Cam-Clay IX constitutive framework that explicitly recognizes the inherent heterogeneity of the rock material. Simulation results suggest that creep of the sample is mostly attributed to the viscoplastic deformation of the material away from the indenter tip, and that such response is highly dependent on the stress rate during the loading stage. Furthermore, simulations of triaxial creep indicate that creep behavior of the bulk sample is dominated by the presence of organics and clay constituents, and that such behavior follows a widely used logarithmic law. Throughout this work, we address the issues of heterogeneity across scales, anisotropy arising from the presence of bedding planes, and viscoplasticity of the individual constituents as they relate to the time-dependent properties of the bulk shale sample.

Keywords

Anisotropy, contact mechanics, creep, indentation, shale, transverse isotropy, viscoplasticity

1 Introduction

Shale is a highly heterogeneous material composed of hard crystalline aggregates (quartz, feldspar, pyrite), and soft nanoporous matrix (clay, organic materials). The complexity of the material system is evident in experiments on the scales of nanometer (Loucks et al., 2009; Semnani and Borja, 2017; Ulm et al., 2007), micrometer (Bennett et al., 1991; Bornert et al., 2010), and centimeter (Chen et al., 2012; Lonardelli et al., 2007; Valcke et al., 2006). Furthermore, experimental studies have recognized the transverse isotropy of shale resulting from the existence of bedding planes (McLamore and Gray, 1967; Niandou et al., 1997; Xu et al., 2011). Multiscale heterogeneity and transverse isotropy have been studied numerically using recently developed constitutive laws (Borja et al., 2020; Choo et al., 2021; Semnani and White, 2020; Zhang, 2020).

Unlike crystalline rocks that tend to fracture under deformation (Bennett et al., 2016; Bennett and Borja, 2018; Borja and Rahmani, 2012; Tjioe et al., 2012; Tjioe and Borja, 2014, 2015, 2016), shale behaves like clay (Borja and Kavazanjian, 1985; Borja, 1990; Borja and Choo, 2016; de Borst and Duretz, 2020; Han et al., 2020; Lazari et al., 2019; Li et al., 2020; Tafili et al., 2020; Zeng et al., 2020; Zhang et al., 2020; Zhao et al., 2019) in that it exhibits pronounced viscous creep behavior in the laboratory and in the field (Abel and Lee, 1980; Chang and Zoback, 2008; Horsrud et al., 1994; Kabwe et al., 2020). Triaxial creep tests on millimeter-scale samples have been extensively conducted on different types of shale (Almasoodi et al., 2014; Li and Ghassemi, 2012; Mishra and Verma, 2015; Rassouli and Zoback, 2015, 2018). Sone and Zoback's triaxial creep tests (Sone and Zoback, 2013) on a number of shale samples showed that creep responses depended on the orientation of deviatoric loading (i.e., stress difference) relative to the bedding plane, as well as on the magnitude of the deviator stress. They concluded that creep behavior was largely attributed to the pore volume compaction inside clay and organic materials (i.e. soft materials), while the hard materials did not contribute much to creep deformation. However, triaxial creep tests require large shale cores that are difficult to obtain from the field. In addition, triaxial creep tests are time consuming – they typically last days if not months. In a series of triaxial creep tests, Rassouli and Zoback (2018) predicted the long-term behavior of shale samples based on short-term responses, but the predictions were not reliable in some cases.

Recent advances in indentation testing allow the measurement of the mechanical properties and creep behavior of shale samples within a period of several minutes (Bobko, 2008; Gathier, 2008; Kumar, Curtis, et al., 2012; Kumar, Sondergeld, et al., 2012; Liu et al., 2016; Shukla et al., 2013; Ulm et al., 2007). Three-stage (load-hold-unload) nanoindentation tests on different constituents of Bakken shale from North Dakota (Liu, Ostadhassan, Bubach, Dietrich, et al., 2018) revealed that creep deformation of soft materials was seven times larger than that of the hard materials within the same time period. Bennett et al. (2015) conducted nanoindentation and microindentation tests on organic-rich Woodford shale samples from the same core and demonstrated the anisotropy of the shale at both scales. However, little information beyond the elastic modulus and hardness of the material could be extracted from indentation tests, and no information on the stress and strain states could be obtained beneath the indented surface of the sample.

Attempts have been made to link the creep behavior of shale at the nano- and micro-meter scales to the centimeter scale (Mighani et al., 2019; Randall et al., 2009; Vandamme and Ulm, 2009, 2013; Zhang et al., 2014) based on an analytical homogenization method originated from Eshelby's inclusion problem (Eshelby, 1957). In this method, the Mori-Tanaka estimate to the homogenized stiffness tensor of a mixture of multiple elastic materials was extended and applied to viscoelastic materials. Furthermore, the two indentation parameters (i.e., modulus and hardness) were derived through dimensionless similarities, and creep related parameters were further calculated by Laplace transformation in the frequency domain. However, in general these methods cannot account for quantified heterogeneity of the sample, nor can they be extended to the inelastic regime.

Recently, Borja et al. (2020) proposed a two-material constitutive model (i.e., Cam-Clay IX) for the creep behavior of shale that accommodated anisotropy, heterogeneity, and viscoplasticity. In this model, shale was represented as a mixture of a stiffer material and a softer material, each forming a solid frame and occupying the same space through their volume fractions. The model captures the anisotropic creep behavior of Barnett shale as well as the onset of dilative shear bands under various loading rates. We use this constitutive model in this paper as a scale-bridging technique to link the creep phenomena in shale across space and time, i.e. from nanometers to millimeters, and from seconds to days. To this end, we employ an incremental frictionless multi-body contact algorithm based on the Lagrange multipliers method to simulate the indentation process.

A 3D mechanistic simulation of the indentation process allows calibration of the viscosities of the two-material model. We first calibrate the viscosity of the soft frame by simulating the nanoindentation process on clay and kerogen. Once the viscosity of the softer matter has been fixed, we then calibrate the viscosity of the hard frame from data on microindentation tests in which both the softer and harder frames are engaged. Finally, the mechanical properties inferred from indentation testing are used to simulate the creep behavior of a triaxial sample of shale to see how the properties calibrated at the nanoscale upscale to the specimen scale.

2 Theory

This section briefly introduces the two-material constitutive law proposed by Borja et al. (2020) and presents the formulation for nonlinear multi-body contact problems based on the Lagrange multipliers method. We note that by assuming a rigid indenter, the size of the system is significantly reduced because the indenter can now be represented as a one-degree-of-freedom body. We also note that the formulation differs from the conventional one-body contact problem (Frohne et al., 2016; Hüeber and Wohlmuth, 2005; Wriggers, 2004) where the rigid body is a prescribed Dirichlet constraint to the deformable body, and not a Neumann constraint on the rigid body. Throughout the derivation, we keep in mind that the problem involves a diamond Berkovich indenter pushed into the surface of a shale sample, after which the load exerted by the indenter on the shale is held fixed while the shale undergoes creep deformation.

2.1 Constitutive law

The Cam-Clay IX model considers a shale as a mixture of a hard crystalline material M and a soft material m representing clay and organics, with the volume fractions ϕ^{M} and ϕ^{m} approximately equal to each other and $\phi^{\mathrm{M}}+\phi^{\mathrm{m}} = 1$. The problem is not the same as the inclusion problem considered by Hill (1963) in that neither volume fraction is more dominant than the other, and so it is possible to assume that separate solid frames may form for each of the two materials. Since the two frames are continuous, their individual displacement fields must be continuous, and since one frame cannot displace relative to the other frame, their displacement fields must be the same. From a kinematical point of view, this implies that the strains in the two frames must be the same, i.e. $\boldsymbol{\epsilon}_{\mathrm{M}} = \boldsymbol{\epsilon}_{\mathrm{m}} = \boldsymbol{\epsilon}$, where $\boldsymbol{\epsilon}$ is the overall strain tensor. Borrowing the ideas from mixture theory (Borja, 2006), the overall Cauchy stress tensor can be determined from the weighted sum of the intrinsic stress tensors $\boldsymbol{\sigma}_{\mathrm{M}}$ and $\boldsymbol{\sigma}_{\mathrm{m}}$ in the rate form

$$\dot{\boldsymbol{\sigma}} = \phi^{\mathrm{M}} \dot{\boldsymbol{\sigma}}_{\mathrm{M}} + \phi^{\mathrm{m}} \dot{\boldsymbol{\sigma}}_{\mathrm{m}} \, . \tag{1}$$

We assume that the total strain rate tensor $\dot{\boldsymbol{\epsilon}}$ can be decomposed into elastic and viscoplastic parts,

$$\dot{\boldsymbol{\epsilon}} = \dot{\boldsymbol{\epsilon}}^{\mathrm{e}} + \dot{\boldsymbol{\epsilon}}^{\mathrm{vp}} \, . \tag{2}$$

The overall viscoplastic strain rate tensor can then be calculated as

$$\dot{\boldsymbol{\epsilon}}^{\mathrm{vp}} = \mathbb{C}^{\mathrm{e}-1} : \Big(\sum_{\alpha=\mathrm{M,m}} \phi^{\alpha} \mathbb{C}^{\mathrm{e}}_{\alpha} : \dot{\boldsymbol{\epsilon}}^{\mathrm{vp}}_{\alpha} \Big) \, , \tag{3}$$

where $\mathbb{C}^{\mathrm{e}}_{\alpha}$ and $\dot{\boldsymbol{\epsilon}}^{\mathrm{vp}}$ are the tangential elasticity tensor and viscoplastic strain rate tensor for material α, respectively; and $\mathbb{C}^{\mathrm{e}}$ is the overall tangential elasticity tensor calculated as the weighted sum of the tangential elasticity tensors $\mathbb{C}^{\mathrm{e}}_{\mathrm{m}}$ and $\mathbb{C}^{\mathrm{e}}_{\mathrm{M}}$.

The viscoplastic strain rate tensor $\dot{\boldsymbol{\epsilon}}^{\mathrm{vp}}_{\alpha}$ for material α has a form analogous to the flow rule used in rate-independent elastoplasticity (Borja, 2013). Two common forms, one proposed by Perzyna (1966) and the other proposed by Duvaut and Lions (1976), are widely used in the context of over-stress model in which the stress point may lie outside the yield surface. However, the Duvaut-Lions model is not appropriate for the problem of indentation simulation due to the lack of a solution for the inviscid problem when the stress concentrates around the tip of the indenter. Thus, only the Perzyna formulation is employed in the present work.

Transverse isotropy is assumed for the hard frame in both the elastic and viscoplastic responses. We assume a transversely isotropic linear elasticity with five independent elastic parameters for the elastic deformation, and an anisotropic version of the modified Cam-Clay model (Semnani et al., 2016; Zhao et al., 2018; Zhao and Borja, 2019) for the viscoplastic deformation. The soft frame is assumed to be isotropic, using an isotropic linear elasticity model with two elastic constants for the elastic response, and the conventional isotropic modified Cam-Clay model for the viscoplastic response. For further details of the model, including the derivation of the algorithmic tangent operator, we refer the readers to Borja et al. (2020).

We emphasize that the present constitutive model applies to the case where the volume fractions of the two groups (soft and hard) are about the same. This assumption applies, for example, to Barnett and Haynesville shales tested by Sone and Zoback (2013) (see the ternary plot representation of sample material compositions in Figure 1 of their paper), as well as to the shale sample imaged by Curtis et al. (2010). In contrast, the problem of inclusion does not admit a continuous displacement field for the less dominant group, as it only takes a ride with the motion of the more dominant group.

2.2 Multi-body contact formulation

In what follows, we assume that contact between the indenter and the indented surface is frictionless. Consider a two-body contact problem consisting of a master body represented by subscript "1" and a slave body represented by subscript "2" (Wriggers, 2004). We denote the set of all potential contact surfaces between the master and slave bodies as Γ_{c}. For each point $\boldsymbol{x}_2$ on the slave side of Γ_{c}, we define a projected point $\overline{\boldsymbol{x}}_1$ on the potential contact surface on the master side such that $\boldsymbol{x}_2 - \overline{\boldsymbol{x}}_1$ is perpendicular to the surface on the slave side (Figure 1). The strong form of the frictionless contact problem is then given by the following set of equations

$$\left.\begin{aligned} \boldsymbol{\nabla}\cdot\boldsymbol{\sigma}_\alpha + \boldsymbol{f}_\alpha = 0 &\quad \text{in } \Omega_\alpha \\ \boldsymbol{u}_\alpha = \boldsymbol{u}_{\alpha 0} &\quad \text{on } \Gamma_{\alpha\mathrm{d}} \\ \boldsymbol{\sigma}_\alpha\cdot\boldsymbol{n}_\alpha = \boldsymbol{h}_\alpha &\quad \text{on } \Gamma_{\alpha\mathrm{h}} \end{aligned}\right\}, \tag{4}$$

subject to the constraints

$$\left.\begin{aligned} (\boldsymbol{u}_2 - \overline{\boldsymbol{u}}_1)\cdot\boldsymbol{n}_2 - g_0 \leqslant 0 \\ \sigma_{\alpha\mathrm{n}} \geqslant 0 \\ \sigma_{\alpha\mathrm{n}}((\boldsymbol{u}_2 - \overline{\boldsymbol{u}}_1)\cdot\boldsymbol{n}_2 - g_0) = 0 \end{aligned}\right\} \text{ on } \Gamma_{\mathrm{c}}\,, \tag{5}$$

where $\alpha = 1, 2$; g_0 is the initial gap between $\boldsymbol{x}_2$ and $\overline{\boldsymbol{x}}_1$; $\sigma_{\alpha\mathrm{n}} = (\boldsymbol{\sigma}_{\alpha\mathrm{n}}\cdot\boldsymbol{n}_\alpha)\cdot\boldsymbol{n}_\alpha$ is the normal component of traction; and $\overline{\boldsymbol{u}}_1$ is the displacement of point $\overline{\boldsymbol{x}}_1$. Here, we follow the soil mechanics convention and denote compression as positive.

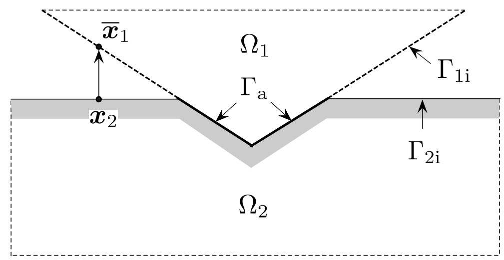

Fig. 1. Schematic plot of contact boundaries.

Let $\lambda_2 \geqslant 0$ and $\overline{\lambda}_1 \geqslant 0$ denote the Lagrange multipliers representing the normal components of traction on the slave and master sides. The potential contact boundary Γ_{c} can be further decomposed into Γ_{a}, the set of boundaries in contact, and $\Gamma_{1\mathrm{i}}$ and $\Gamma_{2\mathrm{i}}$, the set of boundaries not in contact (Figure 1). Here, we further assume that Γ_{a}, $\Gamma_{1\mathrm{i}}$, and $\Gamma_{2\mathrm{i}}$ are known. Later, we shall use the active set strategy (Hintermüller et al., 2002) to determine the contact boundaries. The reformulated strong form is based on the governing equations that assume the contact boundaries are known. These equations take the form

$$\left.\begin{aligned} \boldsymbol{\nabla}\cdot\boldsymbol{\sigma}_\alpha + \boldsymbol{f}_\alpha = 0 &\quad \text{in } \ \Omega_\alpha \\ (\boldsymbol{u}_2 - \overline{\boldsymbol{u}}_1)\cdot\boldsymbol{n}_2 - g_0 = 0 &\quad \text{on } \ \Gamma_{\mathrm{a}} \\ \lambda_2 = 0 &\quad \text{on } \ \Gamma_{2\mathrm{i}} \\ \overline{\lambda}_1 = 0 &\quad \text{on } \ \Gamma_{1\mathrm{i}} \\ \boldsymbol{u}_\alpha = \boldsymbol{u}_{\alpha 0} &\quad \text{on } \ \Gamma_{\alpha\mathrm{d}} \\ \boldsymbol{\sigma}_\alpha\cdot\boldsymbol{n}_\alpha = \boldsymbol{h}_\alpha &\quad \text{on } \ \Gamma_{\alpha\mathrm{h}} \\ \boldsymbol{\sigma}_2\cdot\boldsymbol{n}_2 = -\overline{\boldsymbol{\sigma}}_1\cdot\overline{\boldsymbol{n}}_1 = -\lambda_2\boldsymbol{n}_2 &\quad \text{on } \ \Gamma_{\mathrm{a}} \end{aligned}\right\} . \tag{6}$$

Note from the foregoing equations that $\lambda_2 = \overline{\lambda}_1$ and $\boldsymbol{n}_2 = -\overline{\boldsymbol{n}}_1$ on Γ_{a}. This reformulation is necessary for the derivation of the weak form due to the fact that the widely applied approach of Lagrangian mechanics in contact problems (Wriggers, 2004) is not applicable in the present problem. We remark that for a nonlinear constitutive law such as the one presented in the previous section, the Lagrangian may not be available because of the lack of an explicit expression for the strain energy.

To develop the weak form, we define the sets of trial functions

$$\left.\begin{aligned} \mathcal{S}_u &= \{\boldsymbol{u} | \boldsymbol{u} \in H^1, \boldsymbol{u} = \boldsymbol{u}_{\alpha 0} \text{ on } \Gamma_{\alpha \mathrm{d}} \text{ for } \alpha = 1,\ 2\} \\ \mathcal{S}_\lambda &= \{\lambda | \lambda \in H^0, \lambda = 0 \text{ on } \Gamma_{\alpha \mathrm{i}} \text{ for } \alpha = 1,\ 2\} \end{aligned}\right\}, \tag{7}$$

and the sets of weighting functions

$$\left.\begin{aligned} \mathcal{V}_u &= \{\boldsymbol{\omega} | \boldsymbol{\omega} \in H^1,\ \boldsymbol{\omega} = \boldsymbol{0} \text{ on } \Gamma_{\alpha \mathrm{d}} \text{ for } \alpha = 1,\ 2\} \\ \mathcal{V}_\lambda &= \{\nu | \nu \in H^0,\ \nu = 0 \text{ on } \Gamma_{\alpha \mathrm{i}} \text{ for } \alpha = 1,\ 2\} \end{aligned}\right\}. \tag{8}$$

In what follows, we provide the *linearized* version of the variational equations applicable for the kth Newton iteration at time t_{n+1}, and

$$\boldsymbol{u}_{n+1} = \boldsymbol{u}_n + \sum_{k=1}^{l} \Delta \boldsymbol{u}^k\,, \quad \lambda_{n+1} = \lambda_n + \sum_{k=1}^{l} \Delta \lambda^k\,, \tag{9}$$

where l is the total number of Newton iterations for convergence at the current time step.

The linearized variational equation for the balance of linear momentum for the slave body is

$$
\begin{aligned}
\int_{\Omega_2} \nabla^s \boldsymbol{\omega} : \left.\frac{\partial \boldsymbol{\sigma}_2}{\partial \boldsymbol{u}}\right|_k \cdot \Delta \boldsymbol{u}_2^k \,\mathrm{d}\Omega + \int_{\Gamma_a} \boldsymbol{\omega} \cdot \boldsymbol{n}_2 \Delta\lambda_\mathrm{a}^k \,\mathrm{d}\Gamma
&= \int_{\Gamma_{2\mathrm{h}}} \boldsymbol{\omega} \cdot \boldsymbol{h}_2 \,\mathrm{d}\Gamma + \int_{\Omega_2} \boldsymbol{\omega} \cdot \boldsymbol{f}_2 \,\mathrm{d}\Omega \\
&\quad - \int_{\Omega_2} \nabla^s \boldsymbol{\omega} : \boldsymbol{\sigma}_2^k \,\mathrm{d}\Omega - \int_{\Gamma_\mathrm{a}} \lambda_\mathrm{a}^k \boldsymbol{\omega} \cdot \boldsymbol{n}_2 \,\mathrm{d}\Gamma \,. \qquad (10)
\end{aligned}
$$

The linearized variational equation for the balance of linear momentum for the master body is

$$
\begin{aligned}
\int_{\Omega_1} \nabla^s \boldsymbol{\omega} : \left.\frac{\partial \boldsymbol{\sigma}_1}{\partial \boldsymbol{u}}\right|_k \cdot \Delta \boldsymbol{u}_1^k \,\mathrm{d}\Omega - \int_{\Gamma_\mathrm{a}} \boldsymbol{\omega} \cdot \boldsymbol{n}_2 \Delta\lambda_\mathrm{a}^k \,\mathrm{d}\Gamma
&= \int_{\Gamma_{1\mathrm{h}}} \boldsymbol{\omega} \cdot \boldsymbol{h}_1 \,\mathrm{d}\Gamma + \int_{\Omega_1} \boldsymbol{\omega} \cdot \boldsymbol{f}_1 \,\mathrm{d}\Omega \\
&\quad - \int_{\Omega_1} \nabla^s \boldsymbol{\omega} : \boldsymbol{\sigma}_1^k \,\mathrm{d}\Omega + \int_{\Gamma_\mathrm{a}} \lambda_\mathrm{a}^k \boldsymbol{\omega} \cdot \boldsymbol{n}_2 \,\mathrm{d}\Gamma \,. \qquad (11)
\end{aligned}
$$

The linearized variational equation for the contact constraint is

$$
\begin{aligned}
\int_{\Gamma_\mathrm{a}} \nu \Delta \boldsymbol{u}_2^k \cdot \boldsymbol{n}_2 \,\mathrm{d}\Gamma - \int_{\Gamma_\mathrm{a}} \nu \Delta \overline{u}_1^k \cdot \boldsymbol{n}_2 \,\mathrm{d}\Gamma
&= \int_{\Gamma_\mathrm{a}} \nu [g_0 - (\boldsymbol{u}_2^k - \overline{\boldsymbol{u}}_1^k) \cdot \boldsymbol{n}_2] \,\mathrm{d}\Gamma \,, \qquad (12)
\end{aligned}
$$

where $\lambda_\mathrm{a} = \lambda_2 = \overline{\lambda}_1$ on Γ_a. To determine the sets of boundaries Γ_a, $\Gamma_{1\mathrm{i}}$, and $\Gamma_{2\mathrm{i}}$, the Karush-Kuhn-Tucker (KKT) conditions (Borja, 2013) can be reformulated as

$$
\lambda - \max(0, \lambda + c((\boldsymbol{u}_2 - \overline{\boldsymbol{u}}_1) \cdot \boldsymbol{n}_2 - g_0)) = 0 \quad \text{for } \forall c > 0 \,, \qquad (13)
$$

where σ_n is replaced with the Lagrange multiplier λ. Thus, the set of boundaries in contact, Γ_a, can be determined as (hintermüller et al., 2002)

$$
\Gamma_\mathrm{a} = \{\boldsymbol{x} | \lambda(\boldsymbol{x}) + c((\boldsymbol{u}_2(\boldsymbol{x}) - \overline{\boldsymbol{u}}_1(\boldsymbol{x})) \cdot \boldsymbol{n}_2(\boldsymbol{x}) - g_0)) > 0 \quad \text{for } \forall c > 0\} \,. \qquad (14)
$$

2.3 Numerical implementation

In general, discretization of solids in a contact problem is challenging (Wriggers, 2004). The challenge comes mainly from the fact that the displacement field $\overline{\boldsymbol{u}}_1$ for the projected contact points may not be consistent with the discretization of the master side. If they are not consistent, mapping techniques like node-to-surface, surface-to-surface, and mortar element methods must be applied with extra computation of the mapping procedures. Even if all of the projected contact points coincide with the discretization (a node-to-node contact algorithm), the computational cost associated with creating equally refined meshes for the two bodies may still be high depending on the problem.

However, in simulating an indentation problem, the diamond indenter may be modeled as a rigid body since its stiffness is much higher than that of the indented material. In this paper, we propose a numerical algorithm that deals with the contact problem between a rigid body and a deformable body. More specifically, the displacement of the rigid body is fully represented by only one degree of freedom. In this case, neither the meshing of the rigid body nor the mapping between the contact points from the slave side to the master side is needed. In our model, the entire indenter is modeled with only one degree of freedom u_{r} describing the vertical displacement of the indenter along the direction of indentation. Thus, movements perpendicular to the direction of indentation are all constrained. For a rigid indenter, only the total magnitude of the the normal traction representing the contact force controls the vertical displacement of the indenter, while the actual distribution of the normal traction has no effect. Therefore, without changing the distribution of the normal traction on the slave side, all traction terms on the master side can be combined and shifted to a single node.

The procedure described above reduces the number of elements on the master side to minimum, and greatly simplifies the mapping between the slave and master sides. We note that this approach is different from the one-body contact problem where the rigid body is prescribed through a Dirichlet boundary constraint on the deformable body. It is an appropriate and efficient approach for simulating the problem of creep where the forcing function is a sustained Neumann boundary condition on the rigid body.

Now, Equation (11), which was originally a set of vector equations, has been reduced into a single scalar equation. By simplifying Equations (11) and (12), we arrive at the following system of equations in matrix form

$$\begin{bmatrix} \boldsymbol{K}_2 & \boldsymbol{0} & \boldsymbol{M} & \boldsymbol{0} \\ \boldsymbol{0} & K & \boldsymbol{P} & \boldsymbol{0} \\ \boldsymbol{M}^{\mathsf{T}} & \boldsymbol{P}^{\mathsf{T}} & \boldsymbol{0} & \boldsymbol{0} \\ \boldsymbol{0} & \boldsymbol{0} & \boldsymbol{0} & \boldsymbol{I} \end{bmatrix} \begin{Bmatrix} \Delta \boldsymbol{u}_2^k \\ \Delta u_{\mathrm{r}}^k \\ \Delta \boldsymbol{\lambda}_{\mathrm{a}}^k \\ \Delta \boldsymbol{\lambda}_{2\mathrm{i}}^k \end{Bmatrix} = \boldsymbol{\mathcal{R}}\,, \tag{15}$$

where $\boldsymbol{\Delta u}_2^k \in \mathbb{R}^p$, $\Delta u_{\mathrm{r}}^k \in \mathbb{R}$, $\boldsymbol{\Delta\lambda}_{\mathrm{a}}^k \in \mathbb{R}^q$; and $\boldsymbol{\Delta\lambda}_{2\mathrm{i}}^k \in \mathbb{R}^j$, $p \gg q$ and $p \gg j$. Also, $\boldsymbol{K}_2 \in \mathbb{R}^p \times \mathbb{R}^p$ is the conventional stiffness matrix for the slave body, and is given by

$$\boldsymbol{K}_2 = \int_{\Omega_2} \boldsymbol{B}^{\mathsf{T}} \mathbb{C}_2^{\mathrm{alg}} \boldsymbol{B} \mathrm{d}\Omega\,, \tag{16}$$

where $\mathbb{C}_2^{\mathrm{alg}}$ is the algorithmic tangent operator for the slave body. The sub-matrix $\boldsymbol{M} \in \mathbb{R}^p \times \mathbb{R}^q$ is a rectangular matrix with more rows than columns, and takes the form

$$\boldsymbol{M} = \int_{\Gamma_{\mathrm{a}}} \boldsymbol{N}_{\mathrm{2D}}^{\mathsf{T}}\, \boldsymbol{N}_{\mathrm{3D}}|_{\Gamma_{\mathrm{a}}}\, \mathrm{d}\Gamma\,, \tag{17}$$

where $\boldsymbol{N}_{\mathrm{2D}}$ denotes the shape function matrix used to interpolate the Lagrange multiplier λ, while $\boldsymbol{N}_{\mathrm{3D}}|_{\Gamma_{\mathrm{a}}}$ denotes the matrix used to interpolate the displacement field on the contact surface. If we set $\boldsymbol{N}_{\mathrm{2D}} = \boldsymbol{N}_{\mathrm{3D}}|_{\Gamma_{\mathrm{a}}}$ and apply the Gauss-Lobatto quadrature rule to calculate the integral, then $\boldsymbol{M}$ simplifies to a diagonal matrix (Frohne, 2016)

$$M_{ii} = \int_{\Gamma_{\rm a}} N_i^2 {\rm d}\Gamma, \quad M_{ij} = 0 \text{ for } i \neq j \,. \tag{18}$$

Furthermore, $\boldsymbol{P}$ is a row vector given by the expression

$$\boldsymbol{P} = \mathbf{1}^{\mathsf{T}} \boldsymbol{M} \,, \tag{19}$$

where $\mathbf{1} \in \mathbb{R}^p$ is a column vector with all elements being 1. The null submatrix $\mathbf{0}$ varies in dimension depending on its location in the larger matrix, while K is a positive number with its value depending on the stiffness tensor assigned to the rigid master body. Finally, the fourth row of the block matrix is added to fix the size of the system and minimize memory reallocation.

The nonlinear contact algorithm is summarized in Box 1. We remark that the algorithm can be extended to efficiently solve the contact problem between a rigid body and a nonlinear solid under strain and stress driven conditions. The computational performance of this algorithm will be reported in a future work.

Step 1. Initialize $\Gamma_{\rm c}$, $\boldsymbol{u}$ and λ.

Step 2. Update $\Gamma_{\rm a}$ and $\Gamma_{2{\rm i}}$ from (14).

Step 3. Assemble and solve the system of equations (15).

Step 4. Check if $\|\mathcal{R}\| <$ tolerance and $\Gamma_{\rm a}$ unchanged?

Yes, update $\boldsymbol{u}$, λ, stress and strains. Go to next time step.

Step 5. No, line search on $\boldsymbol{u}$ and λ and go to Step 2.

Box 1. Nonlinear contact algorithm for indentation simulations.

The multi-body contact algorithm and the two-material constitutive model were implemented into an in-house finite element code called GeoScale. The next three sections report the results of numerical simulations conducted in GeoScale to demonstrate the scale-bridging technique that links the creep phenomena in shale from nanometer scale to specimen (millimeter) scale. The first example focuses on capturing the three-stage (load-hold-unload) nano- and micro-indentation responses of a Woodford shale sample, from which the viscous material properties of the hard and soft materials are calibrated. Next, the impact of loading rate and anisotropy on the overall creep responses is investigated during the hold stage of indentation to explain the source of viscous deformation. Finally, long-term triaxial creep behavior of a similar shale is simulated to demonstrate how the formulation upscales to the specimen scale.

3 Indentation responses of Woodford shale

Bennett et al. (2015) conducted nanoindentation and microindentation tests on samples of an organic-rich Woodford shale obtained from the northern flank of the Arbuckle uplift, near the Arkoma Basin, Pontotoc County. Laboratory and field characterization results obtained from the Element Capture Spectroscopy (ECS) showed that the shale sample was composed of hard materials (quartz and pyrite) and soft materials (clay minerals and kerogen) (Abousleiman et al., 2010).

Nanoindentation tests were conducted for three materials, namely, the hard frame (quartz and pyrite), clay, and kerogen. The tests were conducted in both bed-normal (BN) and bed-parallel (BP) directions. Two material parameters were extracted from each nanoindentation test, namely, the effective modulus E_{eff} representing the stiffness, and the hardness H representing the strength. Experimental results showed that the hard frame exhibited anisotropic responses along the two directions, whereas the responses of clay and kerogen were isotropic. Thus, it is natural to describe the hard material as transversely isotropic and the softer clay-kerogen as isotropic. This assumption is consistent with a similar model developed for Barnett shale (Borja et al., 2020).

Microindentation tests were also carried out along the BN and BP directions with larger indentation area and greater indentation depth. In the process, both the hard and soft frames of the material were engaged. On average, the sample tested consisted of nearly 50% hard materials (quartz and pyrite) and 50% soft materials (clay and kerogen) by volume. Thus, the two-material constitutive model combining the transversely isotropic hard frame and the isotropic soft frame is appropriate for modeling the microindented samples.

All indentation tests were performed with a diamond Berkovich indenter with a half angle of 65.27° (Sakharova et al., 2009). Given that the stiffness of diamond is around 10 times higher than that of the hard shale material (Klein and Cardinale, 1993), it is reasonable to simulate the indenter as a rigid body. Contact between the indenter and the indented material was assumed to be smooth, as indicated by Bennett et al. (2015).

In order to obtain the viscosities of the soft and hard frames, we first simulated the nanoindentation creep response of the kerogen using the one material model and took this response as representative of the soft frame (clay-kerogen) creep response. The viscosity was then obtained by fitting the three-stage (load-hold-unload) indentation curve for kerogen. On the other hand, nano-indentation creep tests on the stiffer minerals would not yield any meaningful result since the hold period of 10 minutes would be far too short for the indentation to change noticeably during this period. Instead, we back-figured the viscosity of the hard frame from simulating the microindentation tests along both BN and BP directions. In doing so, both the hard and soft frames were engaged, allowing us to use the two-material model in the simulations.

To characterize the transversely isotropic hard frame material, it is necessary to define a second-order microstructure tensor $\boldsymbol{m}$ as

$$\boldsymbol{m} = \boldsymbol{n} \otimes \boldsymbol{n}\,, \tag{20}$$

where $\boldsymbol{n}$ is the unit vector normal to the plane of isotropy. This tensor defines the general orientation of the plane of isotropy, or bedding plane. The tensorial expression for the elastic tangent modulus can be written in terms of this microstructure tensor as

$$\begin{aligned} \mathbb{C}^e = {} & \lambda \mathbf{1} \otimes \mathbf{1} + 2\mu_T \mathbb{I} + a(\mathbf{1} \otimes \boldsymbol{m} + \boldsymbol{m} \otimes \mathbf{1}) + b\boldsymbol{m} \otimes \boldsymbol{m} \\ & + (\mu_L - \mu_T)(\mathbf{1} \oplus \boldsymbol{m} + \boldsymbol{m} \oplus \mathbf{1} + \mathbf{1} \ominus \boldsymbol{m} + \boldsymbol{m} \ominus \mathbf{1})\,, \end{aligned} \tag{21}$$

where $\mathbf{1}$ is the second-order identity tensor (Kronecker delta) and $\mathbb{I}$ is the rank-four symmetric identity tensor. The tensorial operators $\otimes$, $\oplus$, and $\ominus$ are defined such that $(\bullet \otimes \circ)_{ijkl} = (\bullet)_{ij}(\circ)_{kl}$, $(\bullet \oplus \circ)_{ijkl} = (\bullet)_{jl}(\circ)_{ik}$, and $(\bullet \ominus \circ)_{ijkl} = (\bullet)_{il}(\circ)_{jk}$, see Semnani et al. (2016), Zhao et al. (2018), Zhao and Borja (2019) for further details. Five material constants characterize the elastic properties of the transversely isotropic material. In the above tensorial expression, the constants are λ, μ_T, μ_L, a, and b.

Alternatively, the following five elastic parameters may be used in lieu of the parameters mentioned above: Young's modulus along the BP direction $E^{\mathrm{h}}_{\mathrm{p}}$, Young's modulus along the BN direction $E^{\mathrm{h}}_{\mathrm{n}}$, Poisson's ratio for stress applied and strain measured along the BP direction $\nu^{\mathrm{h}}_{\mathrm{pp}}$, Poisson's ratio for stress applied in the BN and strain measured in the BP directions $\nu^{\mathrm{h}}_{\mathrm{np}}$, and the shear modulus along the BN direction $G^{\mathrm{h}}_{\mathrm{np}}$. For the isotropic soft frame, only the Young's modulus E^{s} and Poisson's ratio ν^{s} are necessary. Here, the superscripts represent the different material frames and the subscripts represent different directions. The Poisson's ratios for the two frames are given in Bennett et al. (2015) and Borja et al. (2020). The Young's moduli can be calculated following the equation (Bennett et al., 2015)

$$E = E_{\mathrm{eff}}(1 - \nu^2)\,, \tag{22}$$

where E, E_{eff} and ν are the general representations of the aforementioned Young's moduli, effective moduli, and Poisson's ratio. The shear modulus $G^{\mathrm{h}}_{\mathrm{np}}$ is assumed to be dependent on the Young's modulus $E^{\mathrm{h}}_{\mathrm{p}}$ and Poisson's ratio $\nu^{\mathrm{h}}_{\mathrm{np}}$ following the expression for isotropic materials

$$G^{\mathrm{h}}_{\mathrm{np}} = \frac{E^{\mathrm{h}}_{\mathrm{n}}}{2(1 + \nu^{\mathrm{h}}_{\mathrm{np}})}\,. \tag{23}$$

We converted the five elastic parameters for the hard frame and the two for the soft frame to the ones adopted by Namani et al. (2012) and Borja et al. (2020). The converted elastic parameters for the hard frame include the Lamé parameter λ^{h}, shear modulus along the BN direction $\mu^{\mathrm{h}}_{\mathrm{n}}$, shear modulus along the BP direction $\mu^{\mathrm{h}}_{\mathrm{p}}$, and the two anisotropy parameters α^{h} and β^{h}. The converted elastic parameters for the soft frame include the Lamé paramter λ^{s}

and the shear modulus μ^{s}. The original and converted elastic parameters are summarized in Table 1.

Table 1. Elastic material parameters for Woodford shale, all in MPa except Poisson's ratios.

hard frame					
original	$E_{\mathrm{p}}^{\mathrm{h}}$	38000	converted	λ^{h}	2900
	$E_{\mathrm{n}}^{\mathrm{h}}$	33000		$\mu_{\mathrm{n}}^{\mathrm{h}}$	13000
	$\nu_{\mathrm{pp}}^{\mathrm{h}}$	0.038		$\mu_{\mathrm{p}}^{\mathrm{h}}$	18000
	$\nu_{\mathrm{np}}^{\mathrm{h}}$	0.19		α^{h}	4100
	$G_{\mathrm{np}}^{\mathrm{h}}$	13000		β^{h}	6900
soft frame					
original	E^{s}	8000	converted	λ^{s}	4600
	ν^{s}	0.3		μ^{s}	3100

In the inelastic regime, we employ the ellipsoidal yield surface of the modified Cam-Clay model but rotate this surface in stress space in the direction that is consistent with the microstructure tensor $\boldsymbol{m}$ to reflect the anisotropy of the hard frame. As demonstrated in Semnani et al. (2016) and Zhao et al. (2018), an alternative way to directly rotating the yield surface in stress space is to consider a fictitious stress configuration $\boldsymbol{\sigma}'$ at which the modified Cam-Clay yield surface may be written in the isotropic form. This is facilitated by a projection tensor $\mathbb{P}$ such that the real Cauchy stress tensor $\boldsymbol{\sigma}$ is mapped to the fictitious Cauchy stress tensor $\boldsymbol{\sigma}'$ according to the equation $\boldsymbol{\sigma}' = \mathbb{P} : \boldsymbol{\sigma}$, where $\mathbb{P}$ is given by (Semnani et al., 2016; Zhao et al., 2018)

$$\begin{aligned} \mathbb{P} = c_1 \mathbb{I} + \frac{c_2}{2}\big(\boldsymbol{m} \oplus \boldsymbol{m} + \boldsymbol{m} \ominus \boldsymbol{m}\big) \\ + \frac{c_3}{4}\big(\boldsymbol{1} \oplus \boldsymbol{m} + \boldsymbol{m} \oplus \boldsymbol{1} + \boldsymbol{1} \ominus \boldsymbol{m} + \boldsymbol{m} \ominus \boldsymbol{1}\big)\,, \end{aligned} \tag{24}$$

in which c_1, c_2, and c_3 are the anisotropy parameters.

The parameters of the anisotropic modified Cam-Clay model include the slope of the critical state line M, the compressibility parameter λ_{p}, and the three anisotropy parameters, c_1, c_2 and c_3, which are all summarized for the hard and soft frames in Table 2. The stress history is defined by the pre-consolidation stress P_{c}, which is also given in the same table. All Cam-Clay parameters are adopted from the numerical simulations of Barnett shale, as reported in the literature (Borja et al., 2020), except that the slope of the critical state line M is estimated from a friction angle of $\phi_{\mathrm{cs}} \approx 36°$ reported by Bennett et al. (2015), along with the standard formula relating M and ϕ_{cs} given in Borja (2013).

Table 2. Cam-Clay parameters for Woodford shale.

harder frame	M^{h}	1.46	softer frame	M^{s}	1.46
	$\lambda_{\mathrm{p}}^{\mathrm{h}}$	0.00013		$\lambda_{\mathrm{p}}^{\mathrm{s}}$	0.0026
	c_1^{h}	0.73		c_1^{s}	1.0
	c_2^{h}	-0.20		c_2^{s}	–
	c_3^{h}	0.40		c_3^{s}	–
	$P_{\mathrm{c0}}^{\mathrm{h}}$	2		$P_{\mathrm{c0}}^{\mathrm{s}}$	35

The setup of the simulation is shown in Figure 2. The indented material was modeled as a cube with a side length of 2 μm for nanoindentation and 50 μm for microindentation. The angle θ denotes the bedding plane orientation in the microindentation simulation, where $\theta = 0°$ represents loading along the BN direction and $\theta = 90°$ represents loading along the BP direction. To simulate the indentation test, the bottom of the cube was fixed and the vertical sides were constrained from lateral movement. The loading protocol followed the test procedure described by Bennett et al. (2015). In the loading stage, a load P was applied as a function of time t on top of the indenter until a predefined maximum indentation depth h was reached. The load-time function is given by

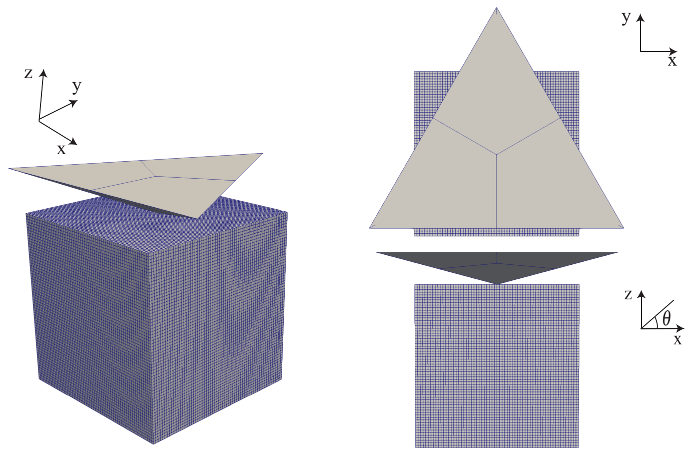

Fig. 2. Finite element model for simulation of indentation tests on Woodford shale.

$$P = P_0 e^{kt} \,. \tag{25}$$

The maximum load was then held for 60 s to allow creep deformation to develop, after which the indenter was unloaded over a period of 20 s. For nanoindentation, P_0 and k were chosen to be 0.022 mN and 0.0156 s^{-1}, respectively, and the maximum indentation depth was 200 nm, while for microindentation, P_0 and k were 1 mN and 0.05 s^{-1}, respectively, and the maximum indentation depth was 5 µm. The calibrated viscosities for the soft and hard frames were determined to be $\eta^{\mathrm{s}} = 1.3 \times 10^{10}\ \mathrm{MPa}^3 \cdot \mathrm{s}$ and $\eta^{\mathrm{h}} = 1.3 \times 10^{13}\ \mathrm{MPa}^3 \cdot \mathrm{s}$, respectively.

We remark that since the load was not applied instantaneously, time-dependent inelastic deformation also developed during the loading stage, which was taken into consideration in the calibration. For the record, however, creep deformation is interpreted herein to be the time-dependent movement of the indenter during the hold stage when the load was held fixed.

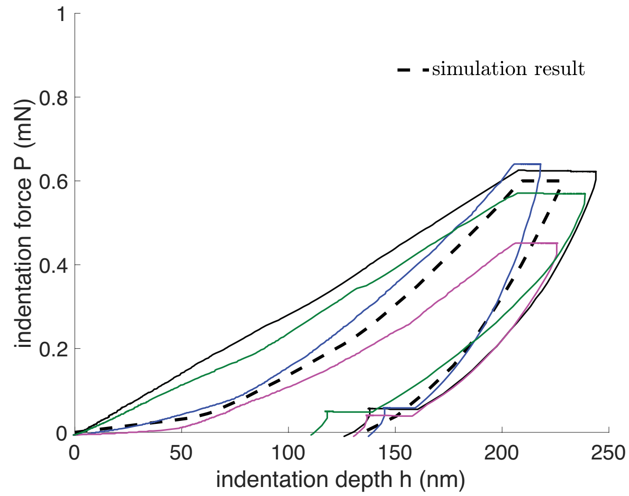

Fig. 3. Nanoindentation on kerogen of Woodford shale: solid lines are experimental results.

The load-indentation responses are shown in Figure 3 for nanoindentation, and in Figure 4 for microindentation simulations along the BN and BP directions. We see that the model captures the material responses during all three stages (load-hold-unload) of the indentation tests quite well. The experimental curves in Figure 3 show more variability in the mechanical responses due to the inherent heterogeneity in material composition of the shale, but the effect of heterogeneity is diminished as both the hard and soft frames were engaged with deeper indentation, see Figure 4. As an aside, the sudden rebound shown by the experimental curves toward the end of the unloading stage is an artifact of the tests and is commonly observed when the indenter disengages from the material being indented. The residual geometry of the microindentation simulation is presented in Figure 5 and compared with a lab photo from Bennett et al. (2015).

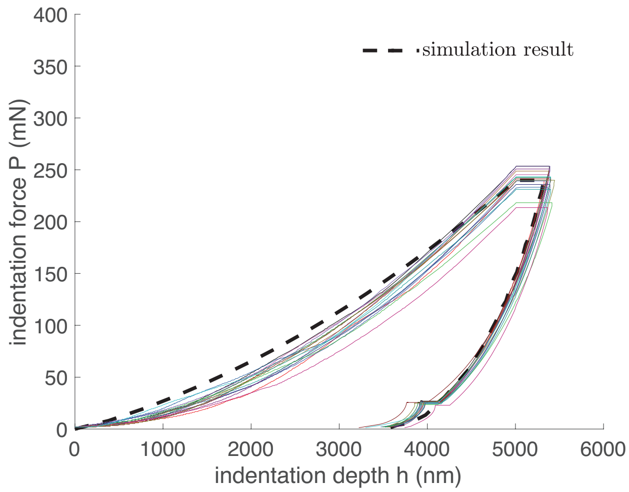

(a)

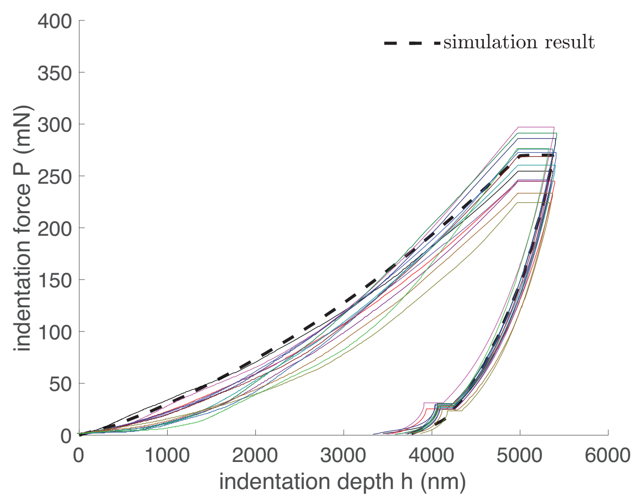

(b)

Fig. 4. Microindentation on Woodford shale: (a) BN direction, (b) BP direction. Solid lines are experimental results.

To summarize, we have obtained the viscoplastic parameters for the hard and soft frames of an organic-rich Woodford shale by simulating nanoindentation tests on the kerogen component and microindentation tests along the BN and BP directions on the rock. These parameters will be used in the following sections to further understand the mechanism of creep during indentation testing, as well as to investigate implications of the calibrated model parameters for creep at the specimen scale.

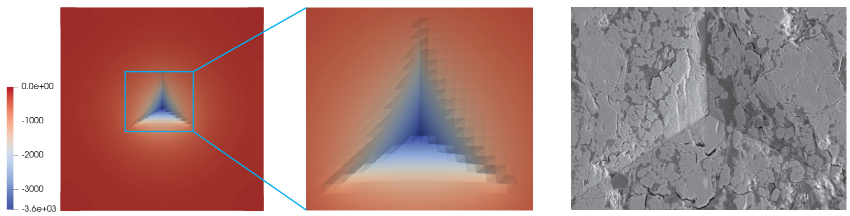

Fig. 5. Post-indented residual geometry from simulation of microindentation versus backscatter electron image adopted from Bennett et al. (2015).

4 Parametric studies

We now perform 2D indentation simulations to study the effect of loading rate and bedding plane orientation on the creep deformation of shale. Ideally, 3D modeling would be desirable for this purpose, much like the modeling described in the previous section. But since we are simply conducting parametric studies in this section, we have reduced the model to 2D plane-strain to avoid the high computing cost associated with 3D simulations. The 2D model used for this purpose is a cross-section cutting through the centroid of the 3D Berkovich indenter as shown in Figure 6. The bedding plane angle θ is also defined in this figure. The resulting 2D triangular indenter has a tip angle of 136.51°, while the side of the block is 2 μm for nanoindentation and 50 μm for microindentation simulations.

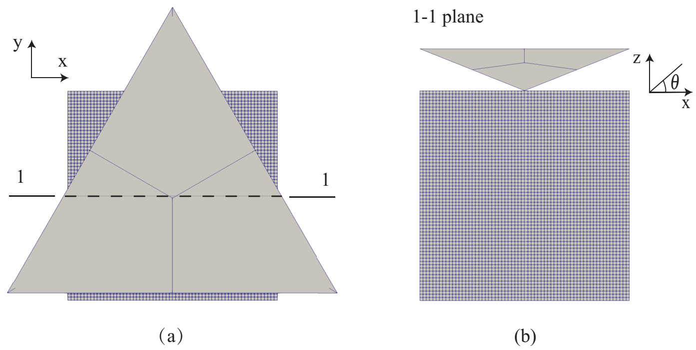

Fig. 6. Model geometry for 2D indentation simulations.

4.1 Effect of loading rate

We first study the effect of loading rate on the creep response of shale. To this end, we consider a one-material constitutive model with an isotropic soft frame and material properties appropriate for the kerogen component of Woodford shale. Indentation loading and creep were simulated as a two-step process. During the loading stage, the load P was increased from 0 to 0.6 mN following the exponential relation

$$P = P_0 e^{\alpha k t}\,, \tag{26}$$

where the loading parameters are $P_0 = 0.022$ mN and $k = 0.0156$ s^{-1}. The loading rate was controlled by the multiplier α, and values of 0.1, 1 and 10 were used in the parametric study. During the creep stage, the load P was held constant at 0.6 mN over a period of 2000 s.

Figure 7 shows the resulting P-h curves for the three chosen values of α. Observe that as the loading rate increases, the depth of indentation decreases, indicating an initially stiffer material response. During the creep stage, however, larger viscoplastic deformations develop in materials that were subjected to higher loading rates.

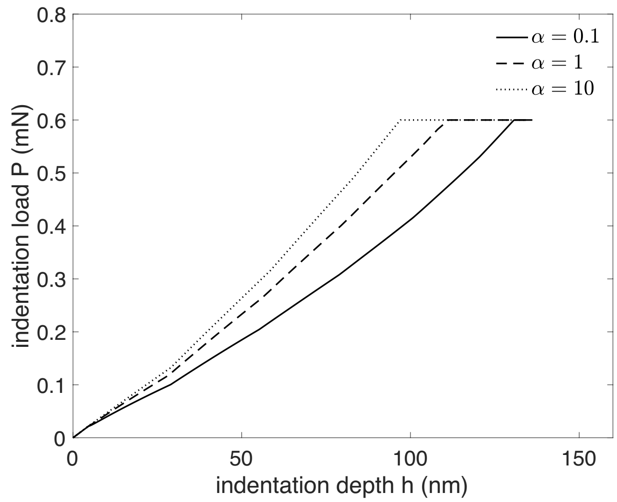

Fig. 7. *P*-*h* curves under different loading rates.

Figure 8 portrays the creep indentation as a function of time and provides insight into the viscoplastic response of the material. In all simulations, the sample was subjected to the same sustained load P. We see that at a higher loading rate, creep deformation develops faster and the indent extends deeper into the rock. The shape of the curve and magnitude of creep deformation for the case $\alpha = 10$ are very similar to those reported by Liu, Ostadhassan, Bubach (2018).

To further understand the mechanism of deformation during the loading and creep stages of indentation, we investigate the evolution of viscoplastic strains within the indented sample. This information is not available from experiments, but fortunately, it can be modeled and investigated numerically.

Figure 9 shows the distribution of the volumetric and deviatoric plastic strains at the beginning and conclusion of the creep stage. The four plots indicate that the deviatoric strain invariant $\|\text{dev}(\boldsymbol{\epsilon}^{\text{vp}})\|$ is more intense and concentrated over a smaller zone, whereas the volumetric strain $\text{tr}(\boldsymbol{\epsilon}^{\text{vp}})$ is less

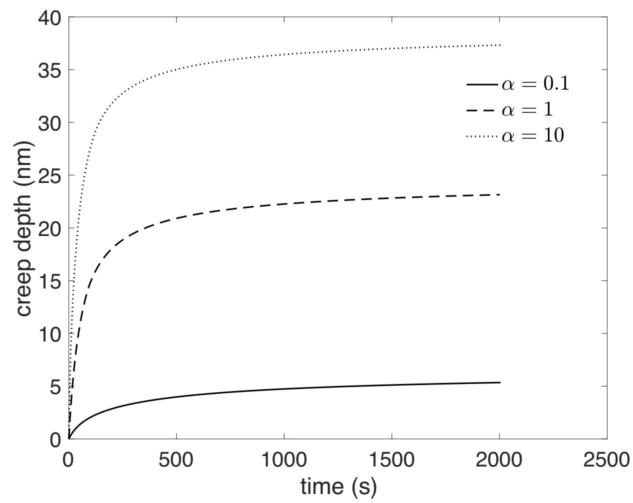

Fig. 8. Indentation creep curves for different loading rates.

intense but more pervasive over a larger region. We recall that the viscoplastic strain rate tensor in the Perzyna model (Perzyna, 1966) is given by the flow rule for the two-material description as (Borja et al., 2020)

$$\dot{\boldsymbol{\epsilon}}^{\mathrm{vp}} = \frac{\langle f_\alpha \rangle}{\eta_\alpha} \frac{\partial f_\alpha}{\partial \boldsymbol{\sigma}} \,, \tag{27}$$

where f_α is the yield function, $\langle \cdot \rangle$ are the Macauley brackets, η_α is the viscosity coefficient, and $\alpha =$ M,m. Near the indenter where the ratio of deviatoric to volumetric stresses (q/p) approaches the slope of the critical state line, inelastic deviatoric strain dominates, but away from the indenter where the stress ratio is close to zero, inelastic volumetric strain pervades.

Figure 10 shows the distribution of the total viscoplastic strain $\|\boldsymbol{\epsilon}^{\mathrm{vp}}\|$ before and after the creep stage. Letters A, B and C correspond to values of $\alpha = 0.1$, 1 and 10, respectively, while numbers 1 and 2 pertain to the start and end of creep. Prior to creep, an increase of α from 0.1 to 10 leads to

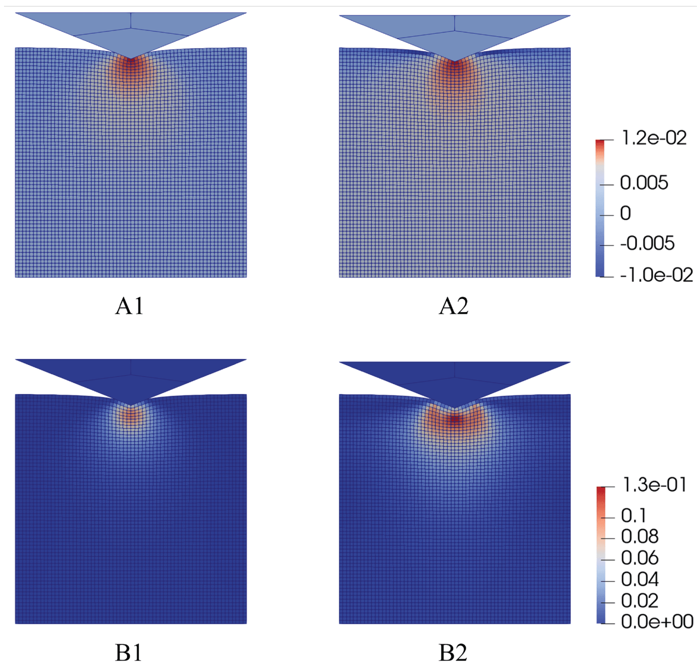

Fig. 9. Volumetric and deviatoric components of viscoplastic strain at the beginning and end of creep. A1 = volumetric/beginning; A2 = volumetric/end; B1 = deviatoric/beginning; B2 = deviatoric/end.

a significant decrease in the magnitude of the viscoplastic strain around the indenter tip, as well as to a reduction in the extent of the inelastic zone. This is consistent with a known feature of viscoplasticity theory in that when the loading rate is high, the deformation of the material is mostly elastic.

Figure 10 also shows that at the conclusion of the creep stage, an inelastic zone forms at a finite distance away from the indenter tip, and not directly below it, even though the total strain experienced by the elements in contact with the indenter is large. This can be attributed to the time-dependent nature of the constitutive model: Under a high loading rate, the elements around the indenter experience elastic deformation. When entering the creep

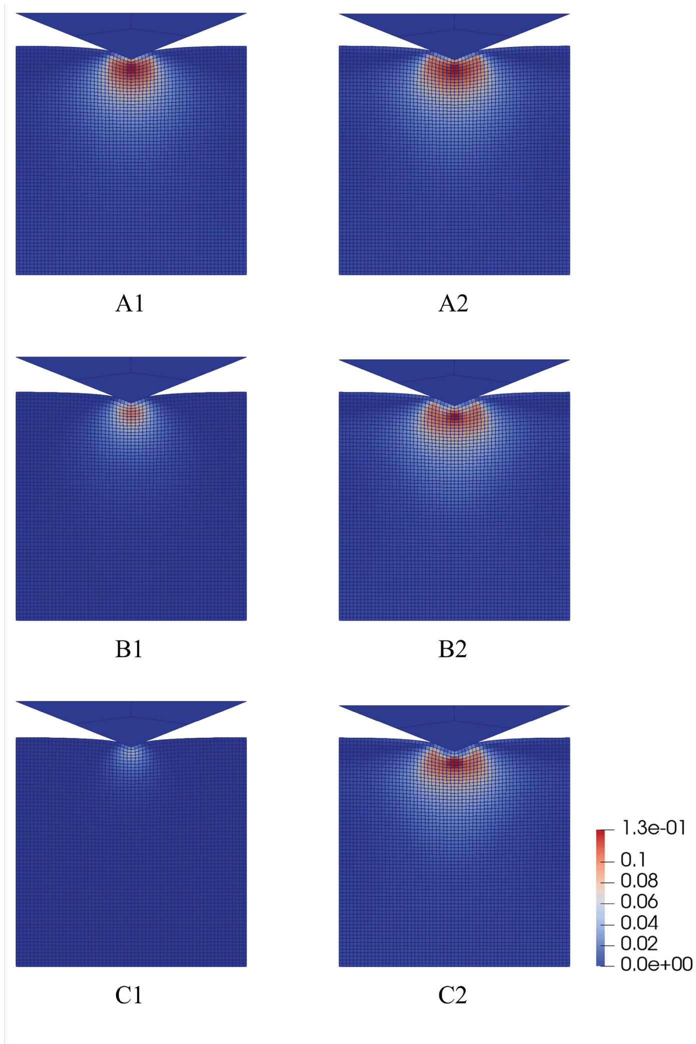

Fig. 10. Total viscoplastic strain $\|\boldsymbol{\epsilon}^{\mathrm{vp}}\|$ for different loading rates and time instants during the creep stage of indentation. Letters A, B, and C are for loading rates of $\alpha = 0.1$, $\alpha = 1$, and $\alpha = 10$, respectively; numbers 1 and 2 pertain to the beginning and end of creep.

stage, however, the over-stress in these elements relaxes to produce inelastic deformation, but the elements in contact with the indenter are constrained by the geometry of the rigid indenter, and so they are unable to deform much in shear.

For a closer look at the time-evolution of the viscoplastic strain and the total stress during the creep stage, we show snapshots of strains and stresses in Figures 11 and 12, respectively. Here, the viscoplastic strain norm $\|\boldsymbol{\epsilon}^{\mathrm{vp}}\|$ and stress norm $\|\boldsymbol{\sigma}\|$ were calculated relative to their initial values at the beginning of the creep stage. The snapshots were taken at three different instants: $t = 100$ s, $t = 500$ s, and $t = 2000$ s, where $t = 0$ denotes the beginning of the creep stage.

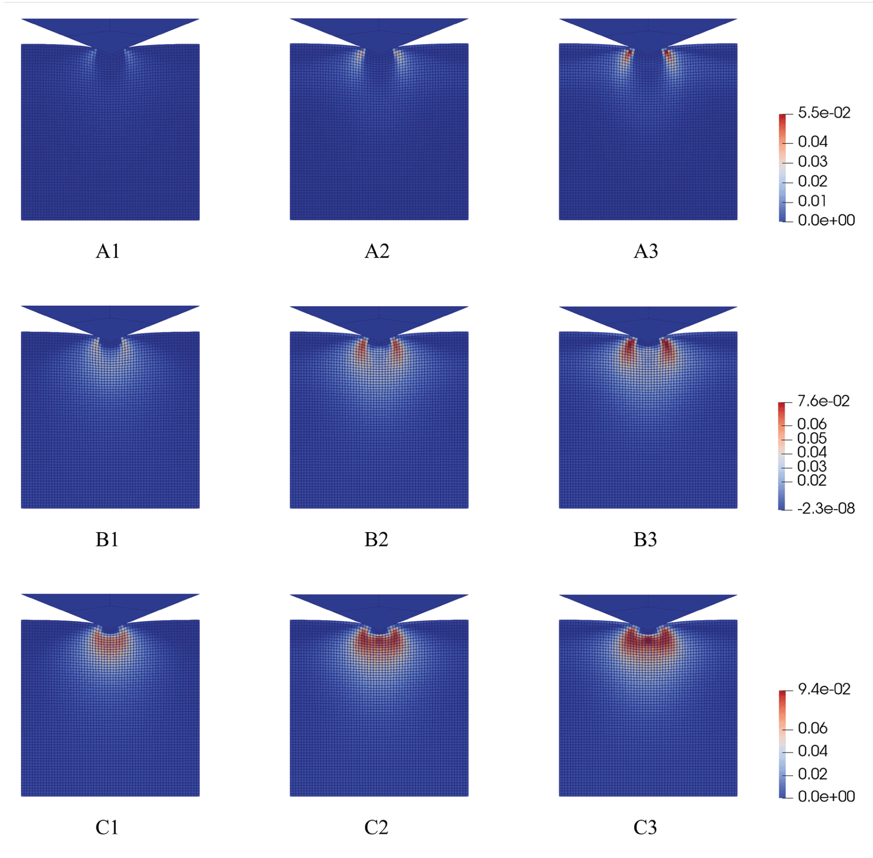

Fig. 11. Creep strains for different loading rates. Letters A, B, and C are for loading rates of $\alpha = 0.1$, $\alpha = 1$, and $\alpha = 10$, respectively; numbers 1, 2, and 3 are for times instants t =100 s, 500 s, and 2000 s, respectively.

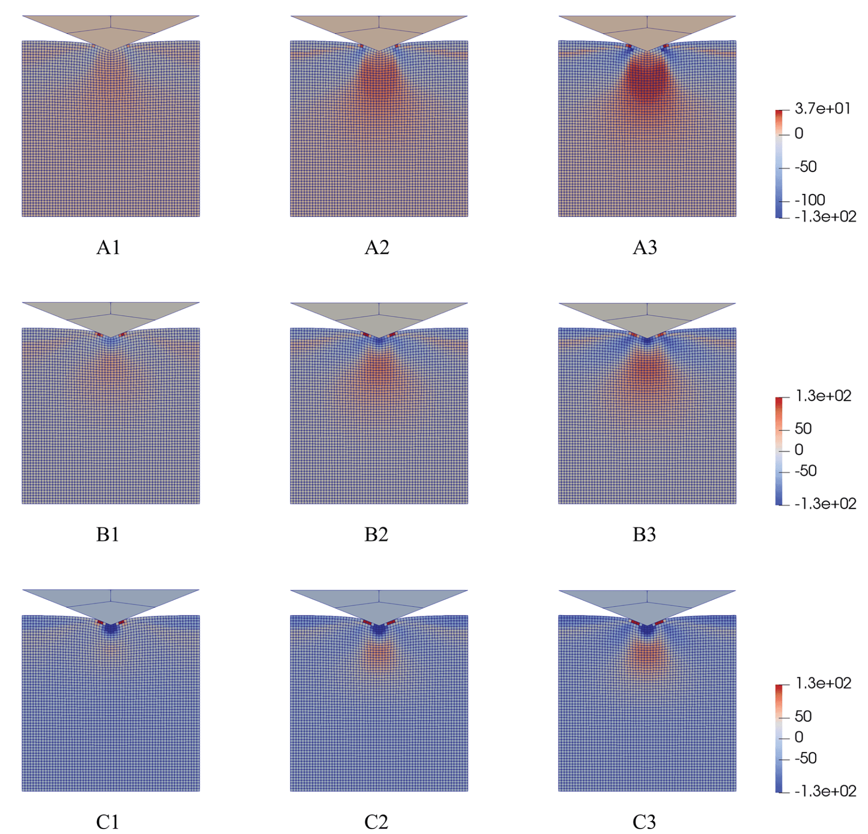

Fig. 12. Change in the stress norm for different loading rates during the creep stage of indentation. Letters A, B, and C are for loading rates of $\alpha = 0.1$, $\alpha = 1$, and $\alpha = 10$, respectively; numbers 1, 2, and 3 are for times instants t =100 s, 500 s, and 2000 s, respectively.

Figure 11 depicts the inelastic zones generated by the indenter load during the creep stage of indentation. For $\alpha = 0.1$, the inelastic zones develop from the top surface of the material on the left and right sides of the indenter, and propagate deeper into the material away from the indenter. For $\alpha = 1$, the inelastic zones appear to merge into a circular region, although the maximum creep intensity remains close to the top surface of the indented material. For $\alpha = 10$, the inelastic zone develops throughout the entire circular region surrounding the indenter.

Figure 12 shows the evolution of the stress norm $\|\boldsymbol{\sigma}\|$ during the creep stage of deformation. For $\alpha = 0.1$, two fan-shaped regions on the two sides of the indent experience a reduction in stress, indicating stress relaxation as the stress point outside the yield surface returns back to the yield surface. This is consistent with the buildup of viscoplastic strains within these same regions, as shown in Figure 11. For $\alpha = 1$ and 10, on the other hand, stresses relax in the zones directly beneath the indenter, which is consistent with Figure 11 in that the inelastic regions concentrate beneath the indenter for these loading rates.

The upshot of Figures 11 and 12 is that the loading rate exerts a significant influence on the way in which the stresses around the indenter redistribute themselves to resist the constant indenter load during the creep stage. When the loading rate is low, the elastic over-stress beneath the indenter is small, and stress relaxation takes place mostly on the sides of the indent. This stress relaxation on the sides must be accompanied by a stress increase beneath the indenter to balance the constant load. This is consistent with the increase in stress at a point in contact with the tip of the indenter for $\alpha = 0.1$, as shown in Figure 13. On the other hand, when the loading rate is high, elastic strains build up beneath the indenter tip prior to creep. Stress relaxation then takes place directly beneath the indenter tip, which is accompanied by a stress increase on the sides of the indent, as well as beneath the indenter but at greater depths, to balance the applied load. This is consistent with the decrease in stresses directly beneath the indenter tip for $\alpha = 1$ and 10, as shown in Figure 13.

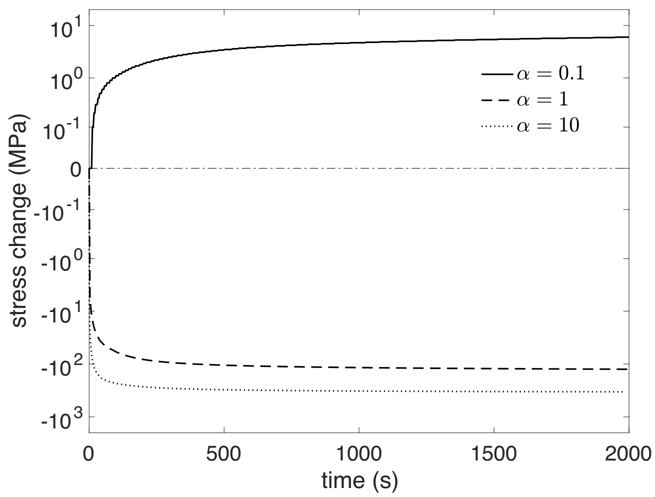

Fig. 13. Change in the stress norm beneath the tip of the indenter under different loading rates during the creep stage.

To summarize, results of the parametric study suggest that creep deformation during the hold period of an indentation experiment arises from the time-dependent strains that develop in the region surrounding the indenter, and not just from the deformation of the material directly in contact with the indenter. Creep deformation depends on the rate at which the indenter load is applied: the faster the loading rate, the greater the creep deformation. The loading rate also impacts the way in which the stresses within the indented material redistribute themselves to balance the applied load.

4.2 Effect of bedding plane orientation

Next, we investigate the effect of cross anisotropy on the creep responses of shale during an indentation test. Anisotropy emanates from the presence of bedding planes, and is accounted for in the model through the hard frame response. We thus consider the two-material model with the soft and hard frames occupying 50% each by volume, and use the material properties for Woodford shale calibrated in Section 3. The sample size is 50 μm × 50 μm, which is comparable to the sample size used for 3D microindentation simulations. The bottom of the sample was fixed and the lateral movements of the vertical boundaries were constrained. The load P at the top of the indenter was increased from 0 to 15 mN over approximately 200 s, following (25), with $P_0 = 0.55$ mN and $k = 0.0156$ s^{-1}. The maximum load was held constant for 2000 s, allowing the sample to creep. Figure 14 shows the resulting creep curves for five different bedding plane angles $\theta = 0°$ (horizontal bedding), 30°, 45°, 60° and 90° (vertical bedding).

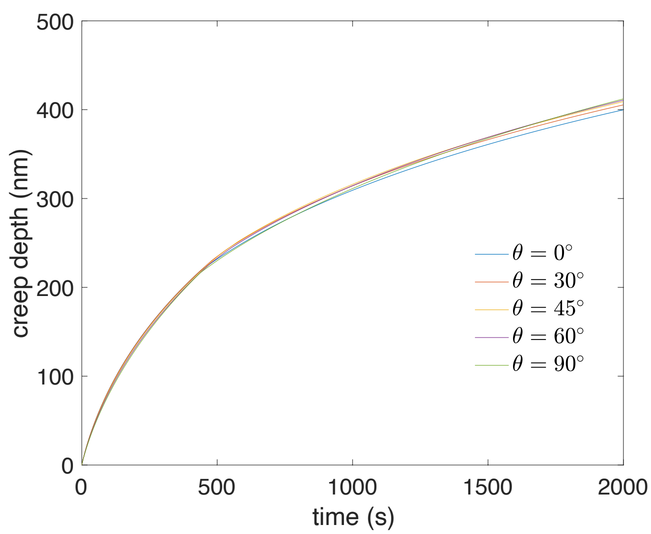

Fig. 14. Indentation creep curves for various bedding plane orientations θ.

The curves shown in Fig. 14 suggest that anisotropy in the creep response does not strongly manifest itself during an indentation experiment, at least within the range of properties considered for Woodford shale. In contrast, as will be shown later in Section 5, strongly anisotropic creep behavior can be reproduced from triaxial creep simulations on the same shale sample with the same material properties. This is due to the fact that indentation test involves localized deformation around the indenter tip, which does not allow the anisotropy of a larger volume to manifest itself. This result is consistent with the experimental results presented by Bennett et al. (2015), which showed that indentation testing has obscured the anisotropic creep response of this shale. The main takeaway from this study is that indentation test is not the right test to investigate anisotropy in creep.

An interesting feature of anisotropic creep during indentation tests is the material flow near the tip of the indenter. When the sample is compressed by the indenter, the material flows from the stronger BP direction to the weaker BN direction. The kinematics of flow can be clearly observed in Figure 15, which shows the scaled displacement vectors for the simulation with $\theta = 45°$.

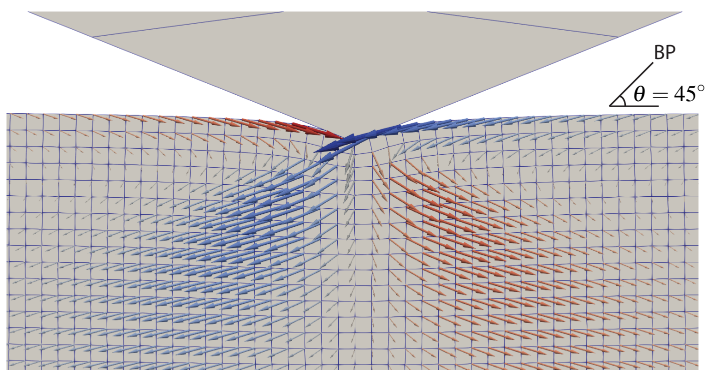

Fig. 15. Displacement vectors during creep for bedding plane orientation $\theta = 45°$.

5 Implications for triaxial creep

In this section, we demonstrate how the model, calibrated from tests on the order of nanometers to micrometers in scale, upscales to the specimen scale. Triaxial creep test is the most common laboratory test for quantifying the time-dependent deformation behavior of geomaterials at the specimen scale. However, this test alone does not distinguish between the creep responses of the individual constituents of a heterogeneous sample of a shale. Neither does it distinguish between the constitutive response of an elementary volume and the structural response of the triaxial sample. The numerical simulations presented in this section could shed some light onto the creep responses of the soft and hard constituents of a shale sample taken individually as well as collectively. Results of the analysis could be useful in interpreting the sources of creep deformation in a heterogeneous sample that would otherwise be difficult to extract from the overall laboratory creep response alone.

We consider once again the two-material Cam-Clay IX model presented in Section 2, along with the calibrated model parameters appropriate for the Woodford shale sample tested by Bennett et al.(2015) and described in Section 3. The finite element mesh for a cylindrical sample with spatially varying hard/soft volume fractions is shown in Figure 16. The sample is 25.4 mm in diameter and 50.8 mm in height, which is approximately the same size as the triaxial sample tested by Sone and Zoback (2013). In principle, the spatial distribution of the hard/soft frame volume fractions can be determined experimentally through a combination of high-resolution imaging and chemical characterization such as through energy dispersive X-ray spectroscopy (EDX), and plotted on ternary plots (see Sone and Zoback (2013)). In the following simulation, however, we generated this type of heterogeneity stochastically, following a normal distribution for the volume fractions ranging from 0.4 to 0.6.

Transverse isotropy was assumed for the hard frame, with the bedding plane orientation described by the angle θ. The bottom end was supported on rollers except for the node at the center, which was supported by a pin to arrest rigid-body lateral translation. A confining pressure of $\sigma_c = 35$ MPa was first applied around the cylinder until the material reached steady state (negligible viscoplastic deformation). Then, a differential stress $\sigma_d = 40$ MPa was applied in the axial direction. The following results pertain to two bedding plane orientations, at $\theta = 90°$ and at $\theta = 0°$.

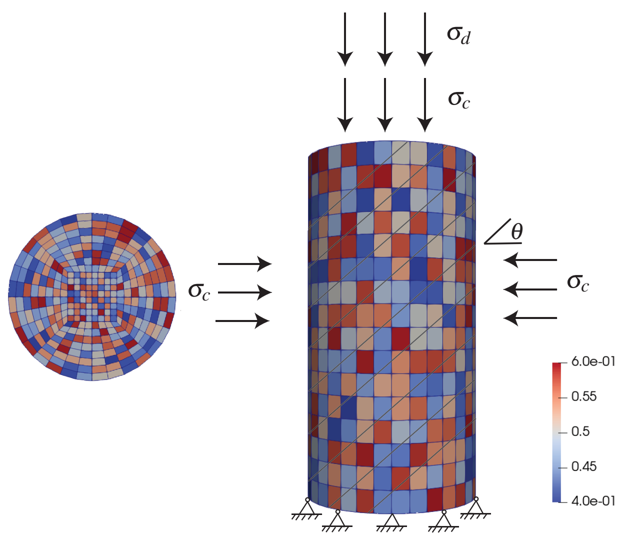

Fig. 16. Setup of the triaxial creep tests.

The axial creep strain after applying the differential stress is reported in Figure 17. Even though the results presented in this figure are only hypothetical and have not been validated experimentally for the specific shale simulated in this example, the creep curves shown in the figure are remarkably very similar to the experimental results reported on Barnett shale by Sone and Zoback (2013) and simulated numerically by Borja et al.(2020). We remark that a noteworthy feature of the present result is that the model parameters used in the simulation were obtained from indentation tests. The fact that the model still produced realistic results for creep at the specimen (millimeter) scale and over several hours of creep, even though the model parameters were calibrated from creep tests that lasted only a few minutes, is encouraging and points to the potential of the framework to bridge scales across space and time.

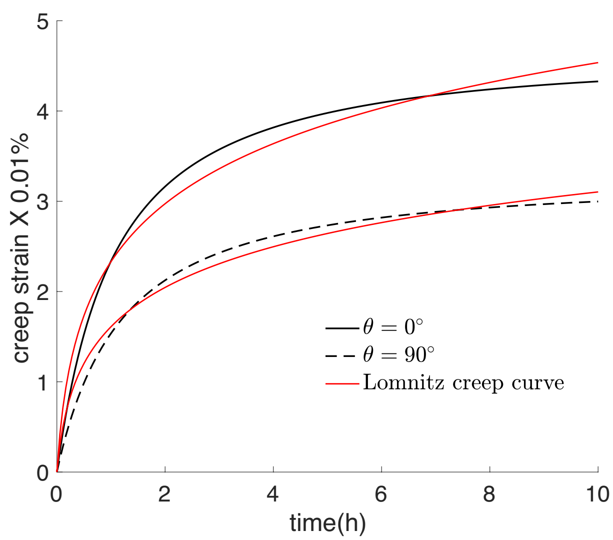

Fig. 17. Axial creep responses from triaxial creep simulations.

Superimposed in Figure 17 are theoretical plots obtained from a widely used phenomenological Lomnitz logarithmic creep law (Lomnitz, 1956), which is given by the analytical equation

$$\epsilon = B \log\left(1 + \frac{t}{\tau}\right), \tag{28}$$

where B and τ are the parameters of the constitutive law. We note that equation (28) only includes the time-dependent part of the original Lomnitz creep law, with the constant component removed from the equation. For $\theta = 0°$, we get $B = 9.97 \times 10^{-5}$ and $\tau = 385$ s; and for $\theta = 90°$, $B = 6.74 \times 10^{-5}$ and $\tau = 364$ s. The discrepancy between the simulated creep responses and the fitted logarithmic curves emanated from the assumption of viscoelasticity in the Lomnitz law, which is a different description of creep response from the one adopted in the present framework.

Because the model can track the evolution of creep strain throughout the domain of the cylindrical sample, it is possible to separate the creep strains in the soft frame from the creep strains in the hard frame and report their evolutions statistically with time. We thus extracted the viscoplastic strain at the Gauss points for each frame and plotted their evolution statistically, as shown in Figure 18. Note that these plots pertain to one stochastic realization, and that the statistical range of creep behavior here refers to the spatial distribution of viscoplastic strain throughout the problem domain. The solid lines represent the mean values, the dark shadows delimit the first and third quartiles (25% and 75%) of the data, and the light shadows mark the range of data. The plots clearly demonstrate that the contribution of the soft frame to the creep response of the cylindrical sample is more than 10 times larger than the contribution of the hard frame, irrespective of the bedding plane orientation. Although it has been recognized that the creep behavior of shale is mostly due to creep of the soft materials (Herrmann et al., 2020; Mighani et al., 2015; Slim et al., 2019; Sone and Zoback, 2013), the methodology presented

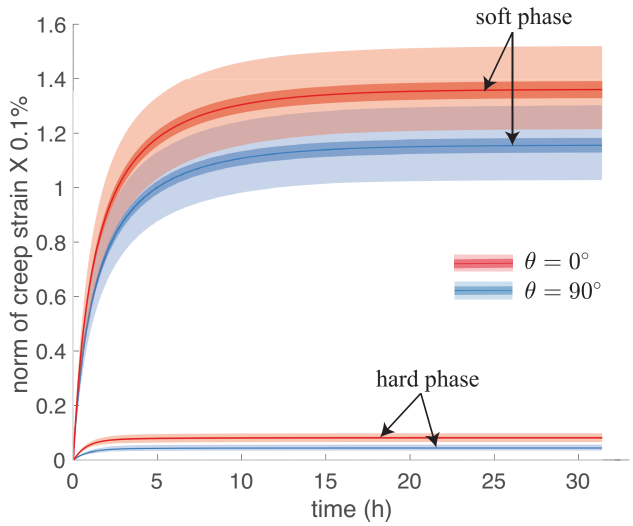

Fig. 18. Statistical plot of triaxial creep responses.

in this work allows (for the first time) a statistical description of the effect of heterogeneity on the creep response of a rock under triaxial condition.

6 Closure

We have presented a scale-bridging technique linking the creep behavior of shale from the nanometer scale to the millimeter scale. At the nanometer scale, nanoindentation simulations were conducted using a one-material elasto-viscoplastic constitutive model representing the response of the softer clay-kerogen matrix. At the micrometer scale, microindentation simulations along the bed-normal and bed-parallel directions were conducted using the recently developed Cam-Clay IX model. From these simulations, we determined the material parameters for an organic-rich Woodford shale. The calibrated model was then used to predict the creep response of a triaxial sample of the same shale in a way that statistically quantifies the contributions of the soft and hard frames to the overall creep response. The schematic of the proposed scale-bridging technique is summarized in Figure 19.

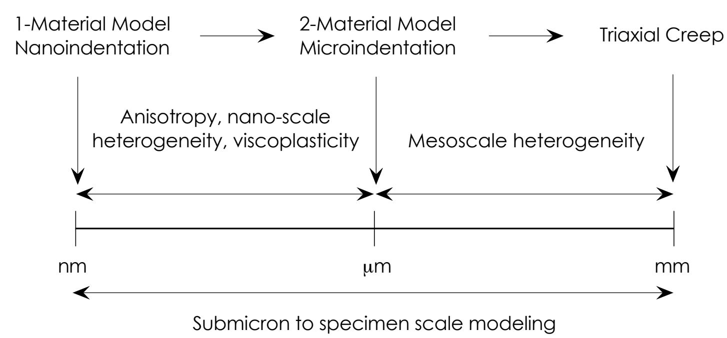

Fig. 19. Scale-bridging technique from nanoscale to millimeter scale.

The main contribution of the work is a framework for shale that links the creep response from nanometer scale to millimeter scale in space, and from a few minutes to several hours of creep responses in time. We are not aware of any framework in the literature that is capable of bridging creep processes over space that spans several orders of magnitude, neither are we aware of any framework that allows calibration of a time-dependent model for rocks from creep tests lasting only a few minutes. The two-material constitutive description facilitated by Cam-Clay IX provides this critical link between the nanoscale and millimeter scale descriptions, see Figure 19. The viscoplastic framework adopted in this model also allows representation of creep processes over time scales several orders of magnitude different. Work is currently underway to investigate the effect of fluid flow on the poromechanics of transversely isotropic rocks (Zhao and Borja, 2020).

Declaration of competing interest

The authors declare that they have no known competing financial interests or personal relationships that could have appeared to influence the work reported in this paper.

Acknowledgements

This work is supported by the U.S. National Science Foundation under Award Number CMMI-1462231 and CMMI-1914780, and by the U.S. Department of Energy, Office of Science, Office of Basic Energy Sciences, Geosciences Research Program, under Award Number DE-FG02-03ER15454.

References

Abel, J.F., Lee, F.T., 1980. Subsidence potential in shale and crystalline rocks (Report No. 80-1072). US Geological Survey. https://doi.org/10.3133/ofr801072.

Abousleiman, Y., Tran, M., Hoang, S., Ortega J.A., Ulm, F.-J., 2010. Geomechanics field characterization of Woodford shale and Barnett shale with advanced logging tools and nano-indentation on drill cuttings. Lead. Edge. 29(6), 730–736. https://doi.org/10.1190/1.3447787.

Almasoodi, M.M., Abousleiman, Y., Hoang, S.K., 2014. Viscoelastic creep of Eagle Ford Shale: Investigating fluid-shale interaction. SPE/CSUR Unconventional Resources Conference–Canada. Society of Petroleum Engineers. SPE-171569-MS. https://doi.org/10.2118/171569-MS.

Bennett, K.C., Berla, L.A., Nix, W.D., Borja, R.I., 2015. Instrumented nanoindentation and 3D mechanistic modeling of a shale at multiple scales. Acta Geotech. 10(1), 1–14. https://doi.org/10.1007/s11440-014-0363-7.

Bennett, K.C., Borja, R.I., 2018. Hyper-elastoplastic/damage modeling of rock with application to porous limestone. Int. J. Solids Struct. 143, 218–231. https://doi.org/10.1016/j.ijsolstr.2018.03.011.

Bennett, K.C., Regueiro, R.A., Borja, R.I., 2016. Finite strain elastoplasticity considering the Eshelby stress for materials undergoing plastic volume change. Int. J. Plast. 77, 214–245. https://doi.org/10.1016/j.ijplas.2015.10.007.

Bennett, R.H., O'Brien, N.R., Hulbert, M.H., 1991. Determinants of clay and shale microfabric signatures: processes and mechanisms, in: Bennett, R.H., Bryant, W.R., Hulbert, M.H., Chiou, W.A., Faas, R.W., Kasprowicz, J., Li, H., Lomenick, T., OBrien, N.R., Pamukcu, S., Smart, P., Weaver, C.E., Yamamoto, T. (Eds.), Microstructure of Fine-Grained Sediments. Springer, New York, NY, pp. 5–32.

Bobko, C.P., 2008. Assessing the mechanical microstructure of shale by nanoindentation: The link between mineral composition and mechanical properties. PhD thesis, Massachusetts Institute of Technology, Cambridge, Massachusetts.

Borja, R.I., 1990. Cam-Clay plasticity, Part 1: Implicit integration of elasto-plastic constitutive relations. Comput. Methods Appl. Mech. Eng. 78, 49–72. https://doi.org/10.1016/0045-7825(90)90152-C.

Borja, R.I., 2006. On the mechanical energy and effective stress in saturated and unsaturated porous continua. Int. J. Solids Struct. 43(6), 1764–1786.

https://doi.org/10.1016/j.ijsolstr.2005.04.045.

Borja, R.I., 2013. Plasticity: Modeling & Computation. Springer, Berlin-Heidelberg.

Borja, R.I., Choo, J., 2016. Cam-Clay plasticity. Part VIII: A constitutive framework for porous materials with evolving internal structure. Comput. Methods Appl. Mech. Eng. 309, 653–679. https://doi.org/10.1016/j.cma.2016.06.016

Borja, R.I., Kavazanjian, E. Jr., 1985. A constitutive model for the stress-strain-time behaviour of 'wet' clays. Géotechnique. 35, 283–298. https://doi.org/10.1680/geot.1985.35.3.283.

Borja, R.I., Rahmani, H., 2012. Computational aspects of elasto-plastic deformation in polycrystalline solids. J. Appl. Mech. 79(3),031024-1–031024-9. https://doi.org/10.1115/1.4005898

Borja, R.I., Yin, Q., Zhao, Y., 2020. Cam-clay plasticity. part ix: On the anisotropy, heterogeneity, and viscoplasticity of shale. Comput. Methods Appl. Mech. Eng. 360, 112695. https://doi.org/10.1016/j.cma.2019.112695

Bornert, M., Vales, F., Gharbi, H., Nguyen Minh, D., 2010. Multiscale full-field strain measurements for micromechanical investigations of the hydromechanical behaviour of clayey rocks. Strain. 46(1), 33–46. https://doi.org/10.1016/j.cma.2019.112695.

Chang, C., Zoback, M.D., 2008. Creep in unconsolidated shale and its implication on rock physical properties. The 42nd US Rock Mechanics

Symposium, San Francisco, California.

Chen, L., Shao, J., Zhu, Q.-Z., Duveau, G., 2012. Induced anisotropic damage and plasticity in initially anisotropic sedimentary rocks. Int. J. Rock Mech. Min. Sci. 51, 13–23. https://doi.org/10.1016/j.ijrmms.2012.01.013.

Choo, J., Semnani, S.J., White, J.A., 2021. An anisotropic viscoplasticity model for shale based on layered microstructure homogenization. Int. J. Numer. Anal. Methods Geomech. 45, 502-520. https://doi.org/10.1002/nag.3167.

Curtis, M.E., Ambrose, R.J., Sondergeld, C.H., Rai, C.S., 2010. Structural characterization of gas shales on the micro- and nano-scales. CUSG/SPE 137693, Canadian Unconventional Resources & International Petroleum Conference, Calgary, Alberta, Canada. https://doi.org/10.2118/137693-MS.

de Borst, R., Duretz, T., 2020. On viscoplastic regularisation of strain-softening rocks and soils. Int. J. Numer. Anal. Methods Geomech. 44, 890–903. https://doi.org/10.1002/nag.3046

Duvaut, G., Lions, J.L., 1976. Inequalities in Mechanics and Physics. Springer, Berlin-Heidelberg.

Eshelby, J.D., 1957. The determination of the elastic field of an ellipsoidal inclusion, and related problems. Proc. R. Soc. Lond. A Math Phys. Sci. 241(1226), 376–396. https://doi.org/10.1098/rspa.1957.0133.

Fischer-Cripps, A.C., 2004. Nanoindentation. Springer-Verlag, New York.

Frohne, J., Heister, T., Bangerth, W., 2016. Efficient numerical methods for the large-scale, parallel solution of elastoplastic contact problems. Int.

J. Numer. Methods Eng. 105(6), 416–439. https://doi.org/10.1002/nme.4977.

Gathier, B., 2008. Multiscale strength homogenization: Application to shale nanoindentation. PhD thesis, Massachusetts Institute of Technology, Cambridge, Massachusetts.

Han, J., Yin, Z.-Y., Dano, C., Hicher, P.-Y., 2020. Cyclic and creep combination effects on the long-term undrained behavior of overconsolidated clay. Acta Geotech. https://doi.org/10.1007/s11440-020-01078-5

Herrmann, J., Rybacki, E., Sone, H., Dresen, G., 2020. Deformation experiments on Bowland and Posidonia shale—Part II: Creep behavior at in situ $p_c - T$ conditions. Rock Mech. Rock Eng. 53(2), 755–779. https://doi.org/10.1007/s00603-019-01941-2.

Hill, R., 1963. Elastic properties of reinforced solids: some theoretical principles. J. Mech. Phys. Solids. 11(5), 357–372. https://doi.org/10.1016/0022-5096(63)90036-X.

Hintermüller, M., Ito, K., Kunisch, K., 2002. The primal-dual active set strategy as a semismooth Newton method. SIAM J Optim. 13(3), 865–888. https://doi.org/10.1137/S1052623401383558.

Horsrud, P., Holt, R.M., Sonstebo, E.F., Svano, G., Bostrom, B., 1994. Time dependent borehole stability: Laboratory studies and numerical simulation of different mechanisms in shale. Rock Mechanics in Petroleum Engineering, Society of Petroleum Engineers, SPE-28060-MS. https://doi.org/10.2118/28060-MS.

Hüeber, S., Wohlmuth, B.I., 2005. A primal–dual active set strategy for non-linear multibody contact problems. Comput. Methods Appl. Mech. Eng. 194(27-29), 3147–3166. https://doi.org/10.1016/j.cma.2004.08.006.

Kabwe, E., Karakus, M., Chanda, E.K., 2020. Creep constitutive model considering the overstress theory with an associative viscoplastic flow rule. Comput. Geotech. 124, 103629. https://doi.org/10.1016/j.compgeo.2020.103629.

Klein, C.A., Cardinale, G.F., 1993. Young's modulus and Poisson's ratio of CVD diamond. Diam. Relat. Mater. 2(5-7), 918–923. https://doi.org/10.1016/0925-9635(93)90250-6.

Kumar, V., Curtis, M.E., Gupta, N., Sondergeld, C.H., Rai, C.S., 2012. Estimation of elastic properties of organic matter in Woodford shale nanoindentation measurements. SPE Canadian Unconventional Resources Conference. Society of Petroleum Engineers, SPE-162778-MS. https://doi.org/10.2118/162778-MS.

Kumar, V., Sondergeld, C.H., Rai, C.S., 2012. Nano to macro mechanical characterization of shale. SPE Annual Technical Conference and Exhibition. Society of Petroleum Engineers, SPE-159804-MS. https://doi.org/10.2118/159804-MS.

Lazari, M., Sanavia, L., di Prisco, C., Pisanò, F., 2019. Predictive potential of Perzyna viscoplastic modelling for granular geomaterials. Int. J. Numer. Anal. Methods Geomech. 43, 544–567. https://doi.org/10.1002/nag.2876.

Li, J., Tang, Y., Feng, W., 2020. Creep behavior of soft clay subjected to artificial freeze-thaw from multiple-scale perspectives. Acta Geotech. 15, 2849–2864. https://doi.org/10.1007/s11440-020-00980-2.

Li, Y., Ghassemi, A., 2012. Creep behavior of Barnett, Haynesville, and Marcellus shale. 46th US Rock Mechanics/Geomechanics Symposium, American Rock Mechanics Association, ARMA-2012-330.

Liu, K., Ostadhassan, M., Bubach, B., 2016. Applications of nano-indentation methods to estimate nanoscale mechanical properties of shale reservoir rocks. J. Nat. Gas. Sci. Eng. 35, 1310–1319. https://doi.org/10.1016/j.jngse.2016.09.068.

Liu, K., Ostadhassan, M., Bubach, B., 2018. Application of nanoindentation to characterize creep behavior of oil shales. J. Pet. Sci. Eng. 167, 729–736. https://doi.org/10.1016/j.petrol.2018.04.055.

Liu, K., Ostadhassan, M., Bubach, B., Dietrich, R., Rasouli, V., 2018. Nano-dynamic mechanical analysis (nano-dma) of creep behavior of shales: Bakken case study. J. Mater. Sci. 53(6), 4417–4432. https://doi.org/10.1007/s10853-017-1821-z.

Lomnitz, C., 1956. Creep measurements in igneous rocks. J. Geol. 64(5), 473–479. https://doi.org/10.1086/626379.

Lonardelli, I., Wenk, H.R., Ren, Y., 2007. Preferred orientation and elastic anisotropy in shales. Geophys. 72(2), D33–D40. https://doi.org/10.1190/1.2435966.

Loucks, R.G., Reed, R.M., Ruppel, S.C., Jarvie, D.M., 2009. Morphology, genesis, and distribution of nanometer-scale pores in siliceous mudstones of the Mississippian Barnett Shale. J. Sediment. Res. 79(12), 848–861.

https://doi.org/10.2110/jsr.2009.092.

McLamore, R., Gray, K.E., 1967. The mechanical behavior of anisotropic sedimentary rocks. J. Eng. Ind. 89(1), 62–73. https://doi.org/10.1115/1.3610013.

Mighani, S., Bernabé, Y., Boulenouar, A., Mok, U., Evans, B., 2019. Creep deformation in vaca muerta shale from nanoindentation to triaxial experiments. J. Geophys. Res. Solid Earth. 124(8), 7842–7868. https://doi.org/10.1029/2019JB017524.

Mighani, S., Taneja, S., Sondergeld, C.H., Rai, C.S., 2015. Nanoindentation creep measurements on shale. 49th US Rock Mechanics/Geomechanics Symposium, American Rock Mechanics Association, ARMA-2015-148.

Mishra, B., Verma, P., 2015. Uniaxial and triaxial single and multistage creep tests on coal-measure shale rocks. Int. J. Coal Geol. 137, 55–65. https://doi.org/10.1016/j.coal.2014.11.005.

Namani, R., Feng, Y., Okamoto, R., Jesuraj, N., Sakiyama-Elbert, S., Genin, G., Bayly, P., 2012. Elastic characterization of transversely isotropic soft materials by dynamic shear and asymmetric indentation. J. Biomech. Eng. 134(6), 061004. https://doi.org/10.1115/1.4006848.

Niandou, H., Shao, J., Henry, J., Fourmaintraux, D., 1997. Laboratory investigation of the mechanical behaviour of Tournemire shale. Int. J. Rock. Mech. Min. Sci. 34(1), 3–16. https://doi.org/10.1016/S1365-1609(97)80029-9.

Perzyna, P., 1966. Fundamental problems in viscoplasticity. Adv. Appl. Mech. 9, 243–377. https://doi.org/10.1016/S0065-2156(08)70009-7.

Randall, N.X., Vandamme, M., Ulm, F.-J., 2009. Nanoindentation analysis as a two-dimensional tool for mapping the mechanical properties of complex surfaces. J. Mater. Res. 24(3), 679-690. https://doi.org/10.1557/jmr.2009.0149.

Rassouli, F.S., Zoback, M.D., 2015. Long-term creep experiments on Haynesville shale rocks. 49th US Rock Mechanics/Geomechanics Symposium, American Rock Mechanics Association, ARMA-2015-532.

Rassouli, F.S., Zoback, M.D., 2018. Comparison of short-term and long-term creep experiments in shales and carbonates from unconventional gas reservoirs. Rock Mech. Rock Eng. 51(7), 1995–2014. https://doi.org/10.1007/s00603-018-1444-y.

Sakharova, N., Fernandes, J., Antunes, J., Oliveira, M., 2009. Comparison between Berkovich, Vickers and conical indentation tests: A three-dimensional numerical simulation study. Int. J. Solids. Struct. 46(5), 1095–1104. https://doi.org/10.1016/j.ijsolstr.2008.10.032.

Semnani, S.J., Borja, R.I., 2017. Quantifying the heterogeneity of shale through statistical combination of imaging across scales. Acta Geotech. 12(6), 1193–1205. https://doi.org/10.1007/s11440-017-0576-7.

Semnani, S.J., White, J.A., Borja, R.I., 2016. Thermoplasticity and strain localization in transversely isotropic materials based on anisotropic critical state plasticity. Int. J. Numer. Anal. Methods Geomech. 40(18), 2423–2449. https://doi.org/10.1002/nag.2536.

Semnani, S.J., White, J.A., 2020. An inelastic homogenization framework for layered materials with planes of weakness. Comput. Methods Appl. Mech.

Eng. 370, 113221. https://doi.org/10.1016/j.cma.2020.113221.

Shukla, P., Kumar, V., Curtis, M., Sondergeld, C.H., Rai, C.S., 2013. Nanoindentation studies on shales. 47th US Rock Mechanics/Geomechanics Symposium. American Rock Mechanics Association, ARMA-2013-578.

Slim, M., Abedi, S., Bryndzia, L.T., Ulm, F.-J., 2019. Role of organic matter on nanoscale and microscale creep properties of source rocks. J. Eng. Mech. 145(1), 04018121. https://doi.org/10.1061/(ASCE)EM.1943-7889.0001538.

Sone, H., Zoback, M.D., 2013. Mechanical properties of shale-gas reservoir rocks — Part 2: Ductile creep, brittle strength, and their relation to the elastic modulus. Geophys. 78(5), D393–D402. https://doi.org/10.1190/geo2013-0051.1.

Tafili, M., Fuentes, W., Triantafyllidis, T., 2020. A comparative study of different model families for the constitutive simulation of viscous clays. Int. J. Numer. Anal. Methods Geomech. 44, 633–667. https://doi.org/10.1002/nag.3024.

Tjioe, M., Borja, R.I., 2014. Mechanisms of deformation in porous rocks at the grain scale, in: Chau, K.T., Zhao, J. (Eds.). Bifurcation and Degradation of Geomaterials in the New Millennium. IWBDG 2014. Springer Series in Geomechanics and Geoengineering. Springer, Cham. https://doi.org/10.1007/978-3-319-13506-9_16.

Tjioe, M., Borja, R.I., 2015. On the pore-scale mechanisms leading to brittle and ductile deformation behavior of crystalline rocks. Int. J. Numer. Anal. Methods Geomech. 39, 1165–1187. https://doi.org/10.1002/nag.2357.

Tjioe, M., Borja, R.I., 2016. Pore-scale modeling of deformation and shear band bifurcation in porous crystalline rocks. Int. J. Numer. Methods. Eng. 108, 183–212. https://doi.org/10.1002/nme.5208.

Tjioe, M., Rahmani, H., Borja, R.I., 2012. Pore-scale deformation in high-porosity rocks. 46th US Rock Mechanics/Geomechanics Symposium. American Rock Mechanics Association, ARMA-2012-670.

Ulm, F.-J., Vandamme, M., Bobko, C., Alberto-Ortega, J., Tai, K., Ortiz, C., 2007. Statistical indentation techniques for hydrated nanocomposites: Concrete, bone, and shale. J. Am. Ceram. Soc. 90(9), 2677–2692. https://doi.org/10.1111/j.1551-2916.2007.02012.x.

Valcke, S., Casey, M., Lloyd, G., Kendall, J.-M., Fisher, Q., 2006. Lattice preferred orientation and seismic anisotropy in sedimentary rocks. Geophys. J. Int. 166(2), 652–666. https://doi.org/10.1111/j.1365-246X.2006.02987.x.

Vandamme, M., Ulm, F.J., 2009. Nanogranular origin of concrete creep. Proc. Natl. Acad. Sci. 106(26), 10552–10557. https://doi.org/10.1073/pnas.0901033106.

Vandamme, M., Ulm, F.-J., 2013. Nanoindentation investigation of creep properties of calcium silicate hydrates. Cem. Concr. Res. 52, 38–52. https://doi.org/10.1016/j.cemconres.2013.05.006.

Wriggers, P., 2004. Computational contact mechanics, second edition. Springer, Berlin, Heidelberg.

Xu, B., Yuan, Y., Wang, Z., 2011. Thermal impact on shale deformation/failure behaviors—Laboratory studies. 45th US Rock Mechanics/Geomechanics Symposium. American Rock Mechanics Association, ARMA-11-303.

Zeng, T., Shao, J.-F., Yao, Y., 2020. A micromechanical-based elasto-viscoplastic model for the Callovo-Oxfordian argillite: Algorithms, validations, and applications. Int. J. Numer. Anal. Methods Geomech. 44, 183–207. https://doi.org/10.1002/nag.3006.

Zhang, Q., LeRoy, R., Vandamme, M., Zuber, B., 2014. Long-term creep properties of cementitious materials: Comparing microindentation testing with macroscopic uniaxial compressive testing. Cem Concr Res. 58, 89–98. https://doi.org/10.1016/j.cemconres.2014.01.004.

Zhang, G., Chen, C., Zornberg, J.G., Morsy, A.M., Mao, F., 2020. Interface creep behavior of grouted anchors in clayey soils: effect of soil moisture condition. Acta Geotech. 15, 2159–2177. https://doi.org/10.1007/s11440-019-00907-6.

Zhang, Q., 2020. Hydromechanical modeling of solid deformation and fluid flow in the transversely isotropic fissured rocks. Comput. Geotech. 128, 103812. https://doi.org/10.1016/j.compgeo.2020.103812.

Zhao, Y., Semnani, S.J., Yin, Q., Borja, R.I., 2018. On the strength of transversely isotropic rocks. Int. J. Numer. Anal. Methods Geomech. 42(16), 1917–1934. https://doi.org/10.1002/nag.2809.

Zhao, D., Hattab, M., Yin, Z., Hicher, P.-Y., 2019. Dilative behavior of kaolinite under drained creep condition. Acta Geotech. 14, 1003–1019. https://doi.org/10.1007/s11440-018-0686-x.

Zhao, Y., Borja, R.I., 2019. Deformation and strength of transversely isotropic rocks, in: Wu, W. (Ed.), Desiderata Geotech., pp. 237–241. https://doi.org/10.1007/978-3-030-14987-1_28.

Zhao, Y., Borja, R.I., 2020. A continuum framework for coupled solid deformation-fluid flow through anisotropic elastoplastic porous media. Comput. Methods Appl. Mech. Eng. 369, 113225. https://doi.org/10.1016/j.cma.2020.113225.